UNIVERSITY OF CALGARY

The Relationship between the Polar Wind and the Terrestrial Helium Budget

by

Jyotsna Kashyap

A THESIS

SUBMITTED TO THE FACULTY OF GRADUATE STUDIES

IN PARTIAL FULFILMENT OF THE REQUIREMENTS FOR THE

DEGREE OF MASTER OF SCIENCE
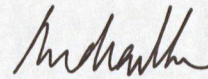
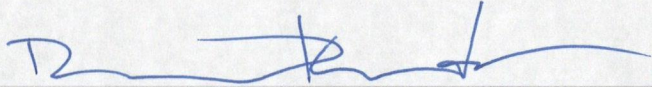DEPARTMENT OF PHYSICS AND ASTRONOMY

CALGARY, ALBERTA

September, 2009

UNIVERSITY OF CALGARY

FACULTY OF GRADUATE STUDIES

The undersigned certify that they have read, and recommend to the Faculty of Graduate Studies for acceptance, a thesis entitled "The Relationship between the Polar Wind and the Terrestrial Helium Budget" submitted by Jyotsna Kashyap in partial fulfilment of the requirements of the degree of MASTER OF SCIENCE.

_____
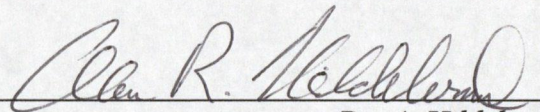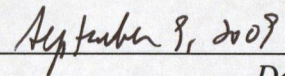Supervisor, Dr. A. W. Yau
Department of Physics and Astronomy

_____
Dr. D. J. Knudsen
Department of Physics and Astronomy

_____
Dr. A. L. Norman
Department of Physics and Astronomy

_____
Dr. A. Hildebrand
Department of GeoScience

_____
Date

Abstract

An apparent inconsistency presently exists in the terrestrial helium budget between the concentration of helium in the atmosphere and the terrestrial helium production and loss rates, the loss rate considered being that due to thermal escape. Escape of He^+ from the polar ionosphere via the polar wind has been suggested to be the most likely candidate to account for the imbalance. In our study, we use a combination of observational data and numerical modeling to estimate the amount of atmospheric helium loss through the polar wind. Using a single particle trajectory tracing model, helium ion trajectories and destinations are simulated over a range of IMF and geomagnetic activity conditions, and the distribution of ion flux to different regions of the magnetosphere is analyzed to quantify the global He^+ outflow. Our calculated escape fraction is ~ 50 to 78% for ion temperatures of 0.1 eV and 0.2 eV, which corresponds to a loss rate of $\sim (3-5) \times 10^{24}$ s^{-1}. This is conceivably sufficient to account for the atmospheric production rate of $\sim (4.5-9.5) \times 10^{24}$ s^{-1} in the literature and therefore explain the current terrestrial helium budget.

Acknowledgements

Table of Contents

List of Tables

List of Figures and Illustrations

List of Symbols, Acronyms and Nomenclature

A	Area
ACE	Advanced Composition Explorer
APL	Applied Physics Laboratory
$\vec{B}$	Magnetic Field
C	Flux integrated over area
C_f	Escape flux
$\vec{\delta}$	Vector from guiding center to particle
∇	Del operator
DE	Dynamics Explorer
DS	Dayside
Dst	Disturbance storm time
DT	Distant tail
ε	Smallness parameter
$\vec{E}$	Electric field
Φ	Electric potential
f	Escape fraction
F	Flux
$\vec{F}$	Force
$\vec{g}$	Gravitational acceleration
G	Gravitational constant (6.67×10^{-11} N m^2 kg^{-2})
GSM	Geocentric Solar Magnetospheric
GT	Gravitationally trapped
H	Higher bulk velocity
HL	Higher latitude
IGRF	International Geomagnetic Reference Field
ILAT	Invariant latitude
IMF	Interplanetary Magnetic Field
IMP	Interplanetary Monitoring Platform
JHU	Johns Hopkins University
λ_L	Longitude
L	Lower bulk velocity
L_t	Thermal escape rate
L_{nt}	Non-thermal escape rate
LL	Lower latitude
μ	Magnetic moment
m	Mass
M_E	Earth's mass (5.98×10^{24} kg)
MLT	Magnetic Local Time
MP	Magnetopause
MSIS	Mass Spectrometer and Incoherent Scatter
n	Density

NSSDC	National Space Science Data Center
ϕ	Azimuth angle
Ψ	Scalar magnetic potential
P	Production rate
P_{dyn}	Dynamic pressure
PA	Pitch Angle
PK	Near-Earth plasma sheet dusk
PN	Near-Earth plasma sheet dawn
PS	Plasma Sheet
PSBL	Plasma Sheet Boundary Layer
q	Charge
Q	Abundance
r	Radial coordinate
r_g	Gyroradius
R	Radial coordinate
R_E	Earth's radius (6371 km)
RG05	Ruohoniemi and Greenwald 2005 model
SMS	Suprathermal Mass Spectrometer
SuperDARN	Super Dual Auroral Radar Network
SWEPAM	Solar Wind Electron Proton Alpha Monitor
θ	Colatitude
τ	Accretion time (of helium)
t	Time
T	Temperature
TAI	Transversely Accelerated Ions
TK	Plasma sheet tail dusk
TN	Plasma sheet tail dawn
T96	Tsyganenko 96 model
UFI	Upflowing Ions
$\vec{v}$	Velocity
ω_g	Gyrofrequency

Chapter One: Introduction

The goal of this research is to study the role of helium ions in the polar wind on the terrestrial helium budget. In order to do this, we make an estimate of the rate of escape of atmospheric helium through the polar wind, and determine whether it can explain the current concentration of helium in the atmosphere.

The subject of the terrestrial helium budget has long been an unresolved question in geophysics. It was found in the sixties that both the concentration and isotopic ratio of helium in the atmosphere were inconsistent with its production and loss rates. The loss rate from thermal Jeans escape and known non-thermal loss mechanisms combined was too small to balance the production rate. This resulted in an apparent imbalance between the known sources and sinks of helium in the atmosphere, leading to the suggestion [*Axford* 1968] that the polar wind might be an important mechanism of helium escape and that the resulting loss rate of helium might be large enough to balance its source rate, accounting for its current concentration. The goal of our research is motivated by this suggestion of *Axford* [1968].

The next section in this chapter provides the relevant scientific background needed to put the work of this project in context. Chapter 2 describes the methodology of our analysis and Chapters 3 and 4 present and discuss the results of the analysis, respectively. Chapter 5 summarizes our conclusions and directions for possible future work.

1.1 Scientific Background

1.1.1 Terrestrial Helium Budget

As explained by *Axford* [1968], the problem of terrestrial helium budget imbalance arises

because the known rates of production and loss of helium fail to account for the current

concentration and isotope ratio in the atmosphere [*MacDonald* 1963]. The production of

He^4 in the Earth's crust is due to the radioactive decay of uranium and thorium. He^3 is

accumulated through solar and galactic cosmic ray He^3 nuclei, and by the decay of

tritium caused by cosmic ray interactions. The rates of production of He^4 and He^3 in the

atmosphere from *Axford* [1968] are $\sim (1\text{--}3) \times 10^6$ atoms $cm^{-2}s^{-1} = (5\text{--}15) \times 10^{24}$ atoms s^{-1}

and $\sim (0.5\text{--}5)$ atoms $cm^{-2}s^{-1} = (2.5\text{--}25) \times 10^{18}$ atoms s^{-1}, respectively. An updated value of

the rate of production (P) of He^4 through degassing from the Earth's crust to the

atmosphere was estimated by *Torgersen* [1989] to be $\sim (0.9\text{--}1.9) \times 10^6$ atoms $cm^{-2}s^{-1} =$

$(4.5\text{--}9.5) \times 10^{24}$ atoms s^{-1}. The global ratios of production are therefore

1(a) $\qquad P(He^4) = (4.5 - 9.5) \times 10^{24}$ atoms s^{-1}

1(b) $\qquad P(He^3) = (2.5 - 25) \times 10^{18}$ atoms s^{-1}

The abundances (Q) of He^4 and He^3 in the atmosphere [*Axford* 1968] are

2(a) $\qquad Q(He^4) = 5.6 \times 10^{38}$ atoms

2(b) $\qquad Q(He^3) = 7 \times 10^{32}$ atoms

From equations (1) and (2) above, it can be seen that the minimum accretion times (τ) for

the present He^4 and He^3 abundances in the atmosphere are

3(a) $\qquad \tau(He^4) = \dfrac{Q(He^4)}{P(He^4)} = (1.9 - 3.9) \times 10^6 \text{ years}$

3(b) $\qquad \tau(He^3) = \dfrac{Q(He^3)}{P(He^3)} = (0.9 - 8.9) \times 10^6 \text{ years}$

In comparison, the average rates of thermal escape (L_t) from the atmosphere [*MacDonald* 1963] are

4(a) $\qquad L_t(He^4) = 3 \times 10^{23} \text{ atoms s}^{-1}$

4(b) $\qquad L_t(He^3) = 1.8 \times 10^{19} \text{ atoms s}^{-1}$

As the minimum accretion times of He^4 and He^3 are similar, and $L_t(He^3)$ is within the known range of $P(He^3)$ while $L_t(He^4)$ is a factor of $\sim$ 15 to 32 times smaller than $P(He^4)$, it is obvious that thermal escape of He^4 is not sufficient to account for its present concentration in the atmosphere. Therefore there must be a non-thermal escape mechanism for helium that favours the heavier isotope such that

5(a) $\qquad L_{nt}(He^4) + L_t(He^4) = P(He^4)$

5(b) $\qquad L_{nt}(He^3) + L_t(He^3) = P(He^3)$

Note that in equation (5)

6(a) $\qquad L_{nt}(He^4) \gg L_t(He^4)$

while

6(b) $\qquad L_{nt}(He^3) \sim L_t(He^3)$

and

6(c) $\qquad L_{nt}(He^4) \sim P(He^4)$

The photoionization rate of atmospheric He^4 is $\sim 10 \times 10^{24}$ atoms s^{-1} [*Nicolet* 1961],

which is of the same order as $P(He^4)$. It was therefore suggested that a process involving

helium ions might account for the non-thermal escape of He^4. As the ions would be

trapped in the Earth's geomagnetic field at lower latitudes where the field lines are closed,

the escape would have to occur at higher latitudes, where the field connects to the

interplanetary magnetic field and the field lines extend all the way to the distant tail of the

magnetosphere. Ion composition observations on satellites in the polar ionosphere have

indeed confirmed the presence of an outflow of thermal plasma from the high latitude

ionosphere to the magnetosphere. This phenomenon is called the polar wind and is

explained in section 1.1.4.

1.1.2 The Ionosphere

The ionosphere is the partially ionized layer of the upper atmosphere that extends

upwards from approximately 100 km, separating the Earth's atmosphere from the inner

edge of the magnetosphere (described in Section 1.1.3), which contains fully ionized

plasma. The term 'plasma' refers to a partially or fully ionized gas that is electrically

conducting but macroscopically neutral. The plasma density in the ionosphere typically

peaks at approximately 300 km. The neutral constituents of the upper atmosphere

undergo photoionization by solar extreme ultraviolet (EUV) and X-ray radiation;

precipitating magnetospheric particles and cosmic rays can also be important mechanisms

of ionization. A series of charge exchange reactions follow the ionization of the major

neutral components (N_2, O_2 and O). Competing processes of ionization and

recombination result in different balances at different altitudes, latitudes and local times,
depending on the composition of the atmosphere and the prevalent geophysical
conditions. This leads to the formation of a number of ionization layers (D, E and F as
shown in Figure 1.1) that are distinguished by their typical plasma densities and
conductivities, as well as the wavelengths of their dominant absorption. Figure 1.1 shows
the dayside density profiles up to 800 km at 45° N for the principal ionic constituents
during solar maximum.
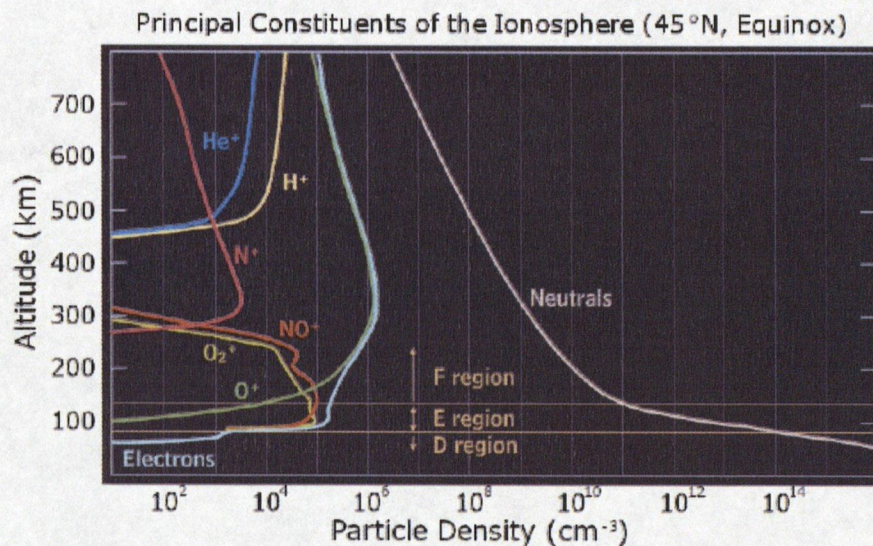
**Figure 1.1. Dayside density profile[1] for the ionosphere during solar maximum, at
45°N.**

At ionospheric altitudes up to a few thousand kilometers, the main source of He$^+$ ions is
the photoionization of neutral helium, and the most important mechanism of loss is
through charge exchange reactions with O_2 and N_2, which convert helium ions back to
neutral helium. The neutral helium, oxygen and nitrogen concentrations and the balance

[1] Taken from http://www.meted.ucar.edu/hao/aurora/iono_const.htm as of July 2009

between the helium ion production and loss processes combine to determine the

abundance of He$^+$, which subsequently affects the polar wind outflow flux and escape

amount. A number of authors have studied He$^+$ density profiles and the characteristics of

outflow from the topside ionosphere. Their work is discussed in Section 1.2.

1.1.3 The Magnetosphere

The Sun expels matter and energy in the form of a supersonic solar plasma outwards into

the heliosphere. The term 'heliosphere' refers to the region of space that is influenced by

the Sun; this region effectively encompasses the whole of the solar system. The

supersonic outflow of plasma from the Sun is referred to as the 'solar wind'. Embedded

in the solar wind is the solar magnetic field, which is also referred to as the interplanetary

magnetic field (IMF). The Earth's internal magnetic field is approximately a magnetic

dipole, with the magnetic 'south' lying near the geographic north pole. The dipole axis is

tilted about 12° away from the geographic rotation axis. While the region of space up to a

few Earth radii (R_E) away from the Earth is dominated by this dipole field, the magnetic

environment beyond that is strongly influenced by the interaction between the Earth's

internal field and the magnetized plasma of the solar wind. The internal field merges with

the IMF, the resultant field being swept anti-sunwards up to hundreds of R_E and shaping

the region into what we call the magnetosphere.

The solar wind slows down when it reaches the dayside region near the Earth and

interacts with the Earth's magnetic field. It flows into a region called the magnetosheath
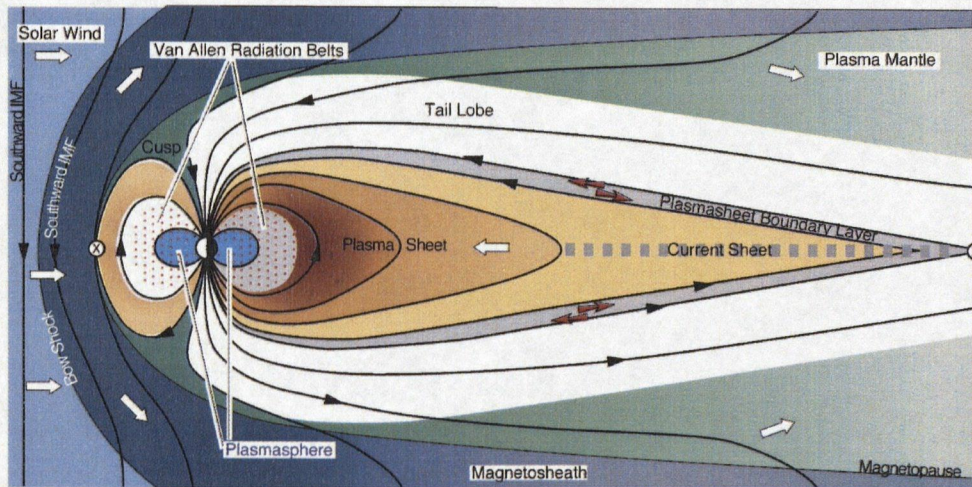
Figure 1.2. The different regions of the magnetosphere. [Taken from *Reiff* 1999]

that is separated from the magnetosphere through a boundary that surrounds it called the magnetopause. This boundary is defined by the equilibrium between the solar wind kinetic pressure and that of the terrestrial magnetic field. The region immediately inside this is the plasma mantle. Equatorward of the plasma mantle on the anti-sunward side lie the tail lobes, which are separated by the plasma sheet and the plasma sheet boundary layer. There are two singularities in the dayside magnetosphere where the closed field lines on the dayside are separated from the open field lines that are swept towards the nightside. These are the polar cusps, created where the magnetic field vanishes when the IMF combines with the terrestrial field and the field lines bifurcate. Solar wind plasma and energetic particles penetrate the magnetosphere freely through the cusp regions. The field lines extending from the cusps to the nightside enclose the magnetotail.

The different regions of the magnetosphere have associated plasma populations with distinct characteristics. The transition from the magnetosheath to the plasma mantle is

characterized by a large drop in plasma density. The plasma sheet contains comparatively dense, hot plasma while that in the tail lobes on either side is cold and rarefied. The plasmasphere lies nearer the earth and parts of it overlap with the Van Allen radiation belts. This region contains trapped, cool, dense plasma that is co-rotating with the Earth. At higher latitudes, magnetic field lines from the auroral regions map to regions in the plasma sheet. The ionosphere acts as a significant source of magnetospheric plasma through a number of outflow processes that are common in the polar regions. These will be discussed in Section 1.1.4.

1.1.4 The Polar Wind

The 'polar wind' refers to the ambipolar[2] outflow of thermal plasma along open magnetic field lines in the polar regions of the earth. The plasma flows from the high-latitude ionosphere to the magnetosphere at supersonic speeds. The ionosphere is believed to be a dominant source of plasma to the magnetosphere. The polar wind is composed primarily of electrons and H^+, O^+ and He^+ ions. Helium is a minor ion component. The existence of the polar wind has been confirmed by observations made by several polar orbiting satellites. The first such measurements date back to the 1970s with Explorer 31 [*Hoffman* 1970] and ISIS 2 [*Hoffman et al.* 1974; *Hoffman and Dodson* 1980]. Other satellites that study polar wind ions are Akebono, POLAR and DE-1 (Dynamics Explorer-1), with observations spanning the altitude range from ~ 1,000 to 50,500 km.

---

[2] An ambipolar process is one that applies equally to both positive and negative ions

The spatial separation between the lighter electrons and the heavier ions in the ionosphere results in an ambipolar electric field directed away from the Earth's gravitational field. The charge separation occurs due to a mass-independent pressure gradient that exists in the polar regions between the lower altitude, high density ionosphere and the higher altitude, lower density regions of the magnetotail. The ambipolar electric field accelerates the ions upwards away from the Earth and then other mechanisms accelerate the particles further along the open magnetic field lines, resulting in parallel ion velocities that increase with altitude, and ion outflow to the magnetotail reaching supersonic speeds.

Outflows in the polar ionosphere occur in two categories [*Yau and Andre* 1997]. The first is bulk ion flows with energies up to a few eV. Examples of these are the polar wind and auroral bulk upflow. The second category is energetic ion outflows, which include upward ion beams and conics. Due to horizontal plasma transport in the polar ionosphere, the various outflow populations sometimes mix and to explain the behaviour of the outflow ions, a combination of different processes have to be examined. Classical polar wind ions in the high altitude polar cap share similar energy and temperature characteristics to ions from sources like auroral bulk upflows and the two sets of ions cannot be distinguished from each other. Therefore, all these ions are included in the expression 'polar wind'. Typical polar wind flows are field aligned and cold ($<10^4$ K), and the parallel (field-aligned) velocities of the different ion species typically vary inversely with the respective ion masses.

1.2 Literature Review

The problem of terrestrial helium budget imbalance was recognized over fifty years ago by a number of authors including *Bates and McDowell* [1957] and *Nicolet* [1957]. A number of the non-thermal processes initially suggested were eventually dismissed as possible mechanisms that might account for the imbalance. They have been reviewed by *Patterson* [1968]. The suggestion that helium escape through the polar wind might provide a solution was originally made by *Axford* [1968]. In a review of the study of helium isotopes in the atmosphere, *Kockarts* [1973] supported the suggestion that the polar wind was the most likely candidate to explain the imbalance between the sources and sinks of atmospheric helium.

Previous work on He^+ outflow is limited. *Banks and Holzer* [1969] solved the continuity and momentum equations for He^+ and found the typical escape flux for He^+ to lie in the range $(2-4) \times 10^6$ $cm^{-2}s^{-1}$. *Lemaire* [1972] developed a collisionless hydrodynamic model of the polar wind including He^+ as one of the components and determined bulk velocity and density distributions. *Mayr* [1972] studied low speed flows in an interhemispheric transport model and also included He^+ in their analysis. *Raitt et al.* [1978a] extended the work of *Banks and Holzer* [1969] to include the energy equation in the steady state in addition to the continuity and momentum equations. They also improved the model by including a number of factors such as the velocity dependence of collision frequencies and the effects of convection electric fields. They considered conditions where He^+ is a minor ion, and investigated the steady state flow of He^+ through a convecting ionosphere

of O^+, H^+, electrons and neutrals N_2, O_2, O, He and H. They considered neutral helium densities typical of both winter and summer hemispheres, and presented density, velocity and temperature profiles for He^+ from 200 to 2,000 km. They considered a range of upper boundary He^+ outflow velocities between 0.1 and 2.5 km/s. The effect of the decreased neutral helium densities from winter to summer was found to scale with the He^+ density linearly. Their computed limiting flux for the winter hemisphere was 5×10^6 $cm^{-2}s^{-1}$, which is consistent with that of *Banks and Holzer* [1969]. The summer flux was a factor of about 20 lower. The difference between the summer and winter fluxes corresponded to the higher neutral density in what is known as the 'winter helium bulge' [*Keating and Prior* 1970], which had not been taken into account in the earlier *Banks and Holzer* [1969] model.

Raitt et al. [1978b] reported improvements to the earlier [*Raitt et al.* 1978a] work. These included modifications to their atmosphere-ionosphere model, and the adoption of the most recent mass spectrometer and incoherent scatter (MSIS) neutral atmospheric density model [*Hedin et al.* 1977a, b] of the neutral atmosphere available at the time. The analysis of *Raitt et al.* [1978b] spanned a range of solar cycle, seasonal and geomagnetic conditions. Season influenced the He^+ density more than any of the other parameters, and reflected the behaviour of the neutral helium density. The effect of magnetic activity was also significant, while solar cycle effects were negligible. The effects of all three parameters on He^+ density were attributed primarily to their effects on the neutral atmosphere and neutral helium density. The density profiles obtained in the study are reproduced in Figure 1.3. For an upper boundary velocity of 0.5 km/s, the limiting fluxes

calculated were between 1.35×10^7 cm^{-2}s^{-1} for low magnetic activity in the winter during

solar maximum, and 0.99×10^5 cm^{-2}s^{-1} for high magnetic activity in the summer during

solar minimum.
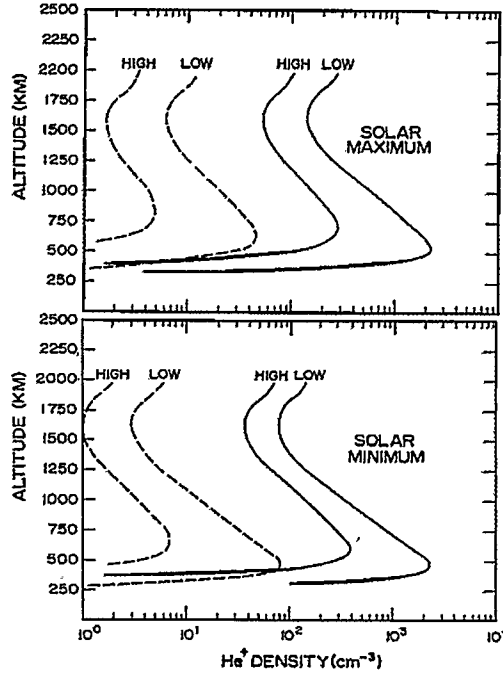
Figure 1.3. Theoretical altitude profiles of He$^+$ densities during solar maximum and solar minimum, for high and low magnetic activity, and summer (dashed curves) and winter (solid curves). [Taken from *Raitt et al.* 1978b]

Hoffman and Dodson [1980] studied polar wind morphology using ISIS 2 measurements

of ion concentrations, flow velocities and fluxes, for periods in 1971 and 1972 around the

solstices and equinoxes at magnetically quiet times. They performed their analysis using

data from ISIS 2 at an altitude of 1,400 km for both winter and summer, by combining

northern and southern hemisphere measurements. Their results confirmed the presence of

an upward flow of He$^+$ over the entire polar region at all times. They found that the He$^+$

fluxes were a factor of 10 higher in the winter than in the summer, following the

behaviour of neutral helium profiles. The equinox flux was bracketed by the summer and winter fluxes, with equinox flux values lying close to the summer values.

Figure 1.4(a) shows their He^+ results at the summer solstice, together with the O^+ results for comparison. The He^+ density decreases in value from the magnetic pole to about 65° invariant latitude (ILAT; the latitude at which a magnetic field line reaches the surface of the Earth, and given by $\cos^{-1}(\sqrt{1/R_L})$ where R_L is the distance in Earth radii to the equatorial crossing of the field line, also known as its L-value) on both the dusk and the dawn sides. The average He^+ flux between the knees at 65° invariant is $1.5 \times 10^6 \text{ cm}^{-2}\text{s}^{-1}$.
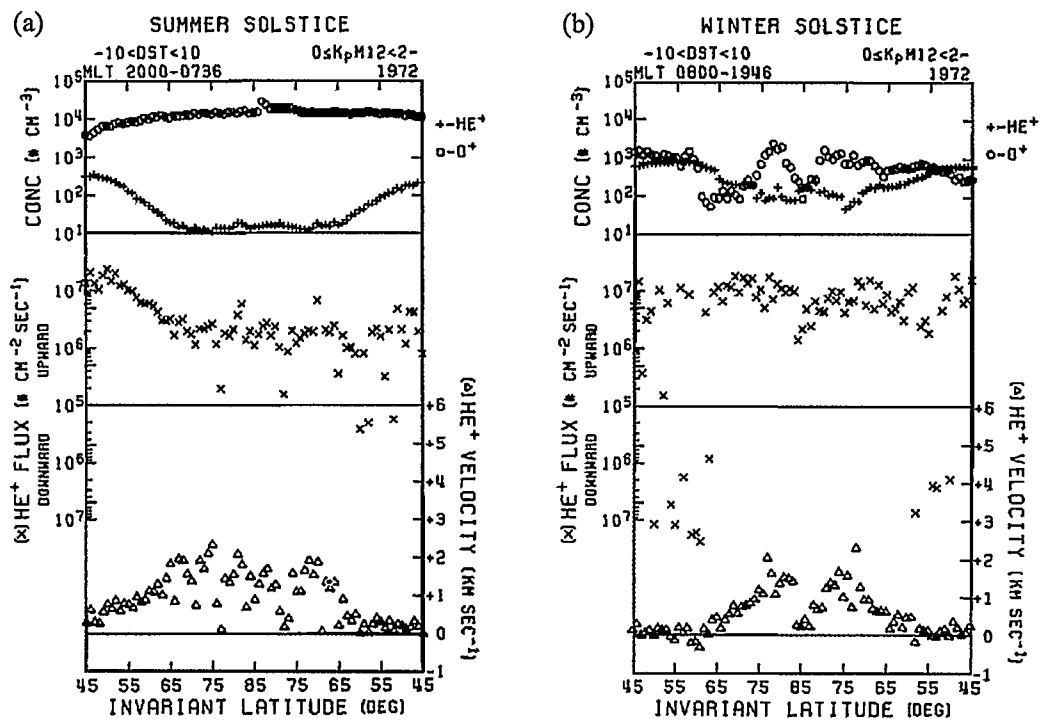
Figure 1.4. He^+ concentrations (O^+ included for comparison), He^+ fluxes and He^+ flow velocities as a function of invariant latitude (with dusk on the left and dawn on the right) during the (a) summer solstice, and (b) winter solstice. [Taken from *Hoffman and Dodson* 1980]

Figure 1.4(b) shows the winter solstice He^+ data. There is a sharp depression in ion velocity and flux at ILAT 85°, but the flux on either side of 85° invariant is $(1-2) \times 10^7$ $cm^{-2}s^{-1}$. A comparison between the theoretical fluxes obtained by *Raitt et al.* [1978b] and the experimental fluxes obtained by *Hoffman and Dodson* [1980] shows very good agreement for winter and low magnetic activity. The difference between the two sets lies in the summer values. We use the experimental set of results in our calculations of escape flux in Chapter 3, Section 3.6.

Collin et al. [1988] performed a statistical survey of energetic He^+ ions observed by DE-1. They derived the spatial and temporal distributions of the particles in the 10 eV to 17 keV energy range. They also studied H^+ and O^+ ions, and found that while the three distributions exhibited the same patterns, He^+ was a minor ion component and was detected only half as often as H^+ and O^+. Several previous studies that had investigated energetic upflowing ions (UFI) had excluded He^+ from their analysis. UFIs were reported to occur in the auroral oval region with the frequency of occurrence increasing with altitude. *Collin et al.* [1988] investigated the importance of energetic helium as a component of the UFIs. They constructed distributions of UFI occurrence frequencies with altitude, invariant latitude and magnetic local time (MLT), dividing the energy ranges into the two intervals (0.01–1.0) keV and (1.0–17.0) keV. The analysis spanned the altitude range from 8,000 to 24,000 km, ILAT from 56° to 88° and all 24 hours of MLT.
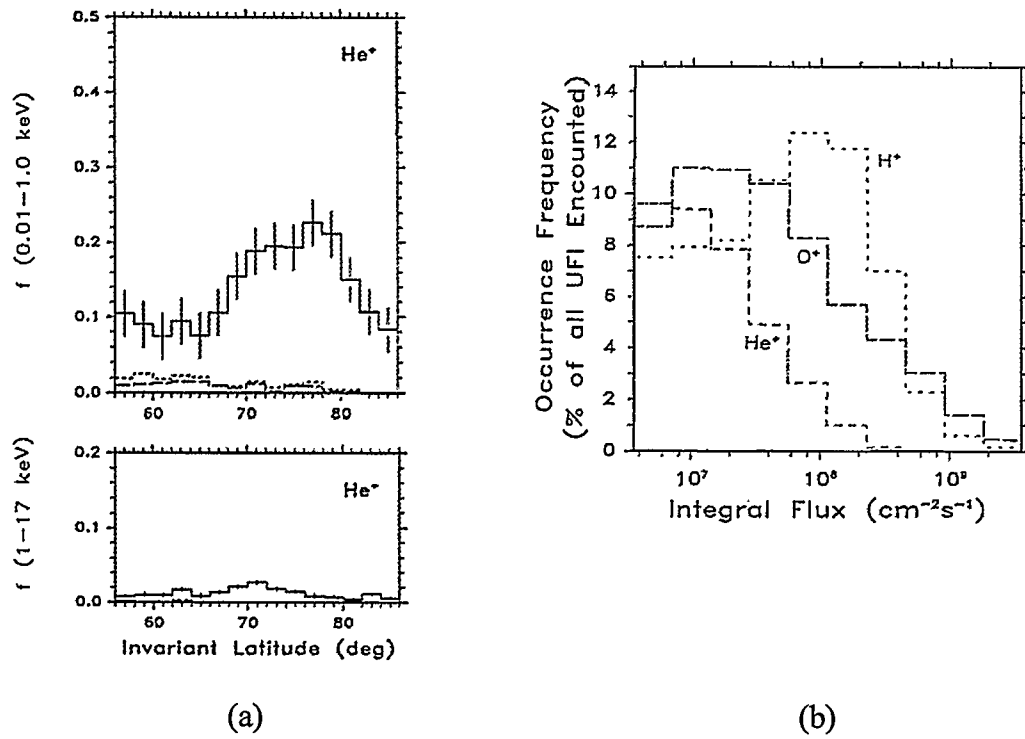
Figure 1.5. (a) Invariant latitude distribution of He^+ UFI occurrence frequency for energy ranges (0.01–1 keV) and (1–17 keV) with the area above the dotted and below the dashed lines representing the frequency of beams and conics, respectively; **(b)** The occurrence frequency distribution of He^+ UFI as a function of the upward integrated flux normalized to altitude 1,000 km. [Taken from *Collin et al.* 1988]

They found that the He^+ UFI were half as frequent and lower in energy than H^+ or O^+ UFI. The H^+ and O^+ distributions were in good agreement to similar profiles presented by *Yau et al.* [1984] who studied energetic outflow in auroral and polar cap regions, also at DE-1 altitudes. The agreement served to validate the He^+ analysis in the *Collin et al.* [1988] paper, despite the fact that they used a more limited data set. The altitude distribution of He^+ UFI occurrence frequency showed the frequencies to lie between 10 to 20% over the range of altitudes considered. The MLT distribution showed a broad dayside peak in the lower energy range while there was a less significant midnight peak

for the higher energy range. The ILAT distribution showed that the He^+ UFI occurred throughout the entire ILAT range considered, and peaked in the auroral zone. The ILAT distribution is shown in Figure 1.5(a), which also contains a subdivision into beams and conics. These are differentiated based on the pitch angle (PA; the angle between a particle's velocity vector and the local magnetic field) distribution of the flux; beams have peak flux between PA 165° and 180° in the northern hemisphere and between 0° and 15° in the southern hemisphere; conics have peak flux between PA 105° and 165° in the northern hemisphere and between 15° and 75° in the southern hemisphere. As the figure shows, the peak for the ions in the lower energy range was found to lie between 75° and 80° ILAT, while the higher energy range peaked at 70° ILAT. Effects of solar activity and magnetic activity were also investigated. The occurrence peak in the auroral zone was found to move to lower latitudes for higher Kp (a planetary index that represents global geomagnetic activity), consistent with observations for other ions made by *Yau et al.* [1984]. Increased solar activity also caused a shift to lower invariant latitudes. The overall UFI occurrence frequency for He^+ increased significantly from lower to higher solar activity, going from 0.12 to 0.21. As noted earlier in Section 1.1.2, He^+ is produced through photoionization by solar radiation, and this dependence is consistent with the suggestions that the neutral atmosphere strongly influences ion outflow, as made by *Yau et al.* [1985a] and *Young et al.* [1982]. Figure 1.5(b) shows the occurrence frequency distribution of He^+ UFI as a function of the upward integrated flux normalized to altitude 1,000 km. The figure shows He^+ UFI fluxes to lie mostly below 3×10^7 $cm^{-2}s^{-1}$, though sometimes exceeding 10^8 $cm^{-2}s^{-1}$. The polar wind limiting flux (the largest value obtained) is 2×10^7 $cm^{-2}s^{-1}$ [*Raitt et al.* 1978b] and 13% of the UFIs were found to have

fluxes higher than this. *Collin et al.* [1988] speculated that the frequent occurrence of He^+ fluxes up to an order of magnitude higher might be due to impulsive or transient rather than sustained events. We do not include He^+ UFIs in our analysis, and the implications of the results obtained by *Collin et al.* [1988] on our study are discussed in Chapter 4.

Lie-Svendsen et al. [1992] used a theoretical approach to study the escape of neutral helium from the terrestrial atmosphere through exothermic charge exchange reactions between He^+ and the major constituents of the atmosphere N_2, O_2 and O. Their study revisited the work of *Maier* [1968], which had proposed charge exchange with N_2 as a mechanism for energetic neutral helium atom production through the reaction of $He^+ + N_2 \rightarrow He + N_2^+ + 9$ eV. *Maier* [1968] suggested that the energy released from this reaction would be a significant source of energetic helium and the atomic He would subsequently be lost from the atmosphere. *Lie-Svendsen et al.* [1992] argued that *Maier* [1968] misunderstood the reaction mechanism and overestimated the kinetic energy available to the He atoms, and overestimated the resulting He^+ densities and escape flux; the exclusion of elastic collisions in *Maier* [1968] was also noted to be another significant drawback. *Lie-Svendsen et al.* [1992] used an interhemispheric plasma transport model to derive the global distributions of He^+ ions versus altitude, latitude and local time for different levels of solar ionization. They applied a kinetic theory approach to treat the elastic collisions between the helium ions and the neutral background. The distribution of the neutral helium escape flux was calculated by combining the ion densities with neutral component densities from the MSIS model of *Hedin* [1987] and estimates of reaction rate coefficients. They found that the escape rates showed significant diurnal and latitudinal

variations, but the global average varied by less than a factor of 3 over a solar cycle. Although these authors found the charge exchange mechanism to be potentially important, they noted that the limited accuracy of the reaction rate coefficients precluded a definitive analysis of the problem.

The work of *Lie-Svendsen et al.* [1996] on minor ion outflow from the terrestrial atmosphere is particularly relevant to our study. Their work was divided into two papers published in 1996. In their first paper, they described their study of minor ion escape using a combination of kinetic theory and moment equations. They argued that the most significant factor that influenced the outflow flux was the transition altitude at which loss due to charge exchange reactions ceased to balance production due to photoionization. This altitude separates the region of chemical equilibrium (below) from where charge exchange loss is no longer significant (above). In the second paper, they expanded on their previous result and developed a method to compute global He^+ escape fluxes for a range of cut-off latitudes separating the regions of open and closed magnetic field lines. They found that a cut-off of 60° or lower would be sufficient to balance the amount of helium produced in the atmosphere. Although our work has concentrated on the same problem and our conclusions are consistent with theirs, our motivation, method of analysis and underlying assumptions differ from theirs. Chapter 4, Section 4.2 contains a more detailed description of their work.

Other studies relevant to our work are those performed by *Abe et al.* [1993] and *Drakou et al.* [1997]. The *Abe et al.* [1993] study reported observations of polar wind ions from

the suprathermal mass spectrometer (SMS) on Akebono for magnetically quiet and disturbed times. They focussed on ions in the polar cap (>80° ILAT) above the collision-dominated altitudes (>2,000 km). Akebono is a polar-orbiting satellite that spans an altitude range of about 1,000 to 10,000 km. SMS collects data for low-energy (up to a few eV) upward ion flows poleward of the auroral oval. Their work described a statistical study of the altitude, invariant latitude, and magnetic local time distributions of the parallel velocities of the respective ion species. The ion velocities were found to increase with altitude; at Akebono apogee, the averaged H^+, He^+, and O^+ velocities were determined to be near 12, 7 and 4 km/s, respectively. The velocity distributions exhibited a day-night asymmetry, with higher ion velocities and temperatures on the dayside. The ion velocity peaked at auroral latitudes at all local times (~ 75° on the dayside and ~ 70° on the nightside). Figure 1.6 shows the polar plot of parallel He^+ ion velocity averaged
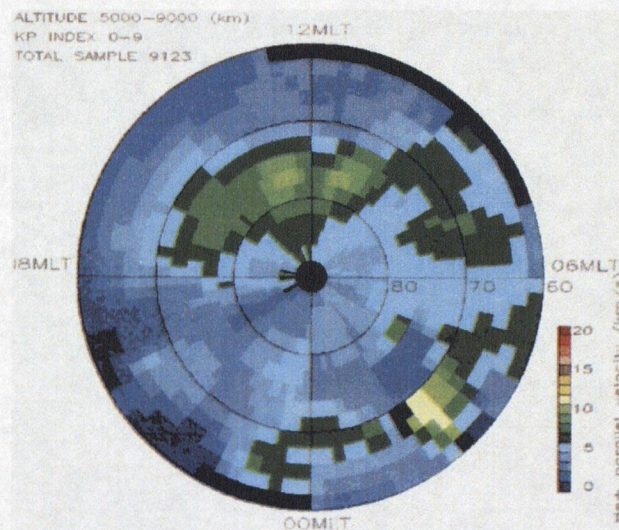
Figure 1.6. Polar plot of averaged parallel ion velocity as a function of ILAT and MLT for He⁺. [Taken from *Abe et al.* 1993]

over 5,000 to 9,000 km as a function of ILAT and MLT. We use an adapted version of this map as input to our model (shown in Chapter 2, Figure 2.4). *Drakou et al.* [1997] presented a method to estimate simultaneously the drift velocity and temperature for thermal ions in the polar ionosphere, using SMS data from a number of Akebono passes at various altitudes, latitudes and local times. Their velocity analysis confirmed the results from previous studies which had reported the existence of significant, supersonic upward flow of He^+ anti-parallel to the magnetic field in the northern hemisphere. Their results also implied that the ion distributions are not Maxwellian, with a higher energy tail component. Their temperature analysis of thermal (energy up to a few eV) ions from 13 representative passes yielded results which indicated that H^+, O^+ and He^+ ions all have low temperatures, in the range of 0.05 to 0.35 eV, with little temperature dependence on altitude, longitude or latitude. We make use of the *Abe et al.* [1993] and the *Drakou et al.* [1997] results as input to our model.

Chapter Two: Methodology

2.1 Overview

2.1.1 Introduction

To achieve our goal of estimating the global escape of helium through the polar wind, we use a combination of computer modeling and observational information derived from existing studies in the literature. In Chapter 1, Section 1.2, we introduced a number of studies that analyze the velocity, temperature and density distributions of polar wind ions. Though the volume of work on the subject of the polar wind is fairly large, helium is a minor ion component and has been relatively less studied. For the objectives of this study, we have synthesized the information in the existing literature into a form that could be used in conjunction with a computer model of single particle trajectories in the magnetosphere to investigate helium outflow. Section 2.1.2 contains a brief history of the use of single particle transport models.

In our study, we simulate individual ion trajectories and destinations and create destination distributions based on the output data from the model. We then perform statistical analysis on the destination distributions, which enables us to estimate the magnitude of the helium escape. The amount that escapes depends strongly on the geophysical conditions and the initial conditions of the particles, and these constitute the

input to the model. For a global estimate, both the geophysical conditions and the initial particle conditions are selected to enable us to define the range of helium escape.

Section 2.1.3 contains an overview of the formulation of the simulations. Section 2.2 develops the equation of motion including the guiding center approximation (in Section 2.2.3) that is solved in the simulation to obtain each particle's trajectory and destination. Section 2.3 discusses the modeling of the fields and Section 2.4 contains the details of the input data sets to the model.

2.1.2 Single Particle Transport Models

Several studies in the past have used the method of tracing single particle trajectories to understand different aspects of the dynamics of outflowing ions in the magnetosphere. *Horwitz and Lockwood* [1985] investigated the transport of ionospheric ions using a two-dimensional kinetic trajectory-based model which included the effects of gravitation, magnetic gradient force, convection electric fields and parallel electric fields. They studied dependences on source energies, convection and parallel electric fields and ion masses. *Cladis* [1986] was the first author to investigate the effects of the convection electric field in regions of magnetic field curvature or changing magnetic field on accelerating ions in the polar ionosphere by implementing a two-dimensional outflow model. *Delcourt et al.* [1989] investigated transport of terrestrial plasma through the magnetosphere by tracing three-dimensional trajectories to examine various ionospheric outflows. In their initial model, the simulations were limited to the region of the

magnetosphere within a geocentric radius of 17 R_E. Subsequently, *Delcourt et al.* [1993, 1994] used an improved model that included the magnetic field further downtail in the magnetosphere, and investigated the circulation of polar wind ions from the high latitude ionosphere to the plasma sheet.

More recent studies that involve particle tracing include the work of *Huddleston et al.* [2005], who examined ionospheric plasma supply to the magnetosphere. Using measured ionospheric source characteristics in conjunction with trajectory code, they studied the supply process and determined that it was sufficient to account for the observed densities and energies in the plasma sheet and magnetotail lobes. *Cully* [2001] and *Cully et al.* [2003b] traced low energy particles from the polar ionosphere and studied the supply of H^+ and O^+ ions to regions extending up to the central plasma sheet. They examined ions associated with all types of outflow, including the polar wind, and performed trajectory traces in the guiding center approximation. Their simulation used the Tsyganenko 1989 [*Tsyganenko* 1989] and Weimer 1995 [*Weimer* 1995] models for the magnetic and electric fields, respectively. They ran simulations for northward and southward IMF, and computed fluxes to different destination regions by weighting the trajectories by outflow rates that were derived from the Akebono ion outflow data collected by *Cully et al.* [2003a].

Howarth [2006] and *Howarth and Yau* [2008] used a single particle transport model to study the outflow of low-energy H^+ and O^+ ions at high latitudes. Their method and code were developed based on the previous work of *Cully* [2001] and *Cully et al.* [2003b].

Their study included ion data from 85 Akebono passes. The simulations used the T96

(Tsyganenko 1996) [*Tsyganenko* 1995; *Tsyganenko and Stern* 1996] and International

Geomagnetic Reference Field (IGRF[3]) models to compute the magnetic field

distributions at the times of the Akebono passes, and the JHU APL (Johns Hopkins

University Applied Physics Laboratory) model based on SuperDARN data to compute

the electric field distributions. Their results were divided by IMF direction to examine the

effects of IMF on the transport of the ions. In this study, we adapt the code kindly

provided to us by the authors of *Howarth and Yau* [2008] by making some necessary

changes related to the method of input to the code and the computing platform the code

was run on, and apply it to He$^+$ ions to study helium outflow. In addition, we apply the

method of *Cully et al.* [2003b] to weight the trajectories by the outflow rates to calculate

the helium escape fluxes.

2.1.3 Formulation of the Simulations

Similar to *Howarth and Yau* [2008], we carry out simulations over a magnetospheric grid

which covers the region of $(X, Y, Z) = (-70$ to $+10$ R_E, -25 to $+25$ R_E, and -30 to $+30$ $R_E)$

in the magnetosphere, where X, Y, Z are in Geocentric Solar Magnetospheric (GSM)

coordinates. The GSM system is a Cartesian coordinate system. The origin lies at the

center of the Earth with the X-axis lying along the direction of the Sun (positive towards

the Sun). The Y-axis is perpendicular to both the X-axis and the Earth's magnetic dipole

---

[3] http://www.ngdc.noaa.gov/IAGA/vmod/igrf.html as of July 2009

(positive towards dusk) and the Z-axis completes the orthogonal triad (positive towards the magnetic pole in the northern hemisphere). The grid is divided into 101 points in each direction which are fixed such that the density of points is closer nearer the Earth, where the fields are stronger. Explicitly, the coordinates at each point are given by

$$(2.1a) \quad X_i = \left(\frac{X_{max} - X_{min}}{i_{max}^a - 1} \right) \times i^a + \left(\frac{X_{min} i_{max}^a - X_{max}}{i_{max}^a - 1} \right) \qquad \forall \, 1 \le i \le i_{max}$$

$$(2.1b) \quad Y_j = \left(\frac{Y_{min}}{1 - \left(\frac{j_{max}}{2} + 1 \right)^b} \right) \times j^b + \left(\frac{Y_{min} \left(\frac{j_{max}}{2} + 1 \right)^b}{\left(\frac{j_{max}}{2} + 1 \right)^b - 1} \right) \qquad \forall \, 1 \le j \le \frac{j_{max}}{2} + 1$$

and $\quad Y_j = -Y_{j_{max} - j + 1} \qquad\qquad\qquad \forall \, \frac{j_{max}}{2} + 2 \le j \le j_{max}$

$$(2.1c) \quad Z_k = \left(\frac{Z_{min}}{1 - \left(\frac{k_{max}}{2} + 1 \right)^c} \right) \times k^c + \left(\frac{Z_{min} \left(\frac{k_{max}}{2} + 1 \right)^c}{\left(\frac{k_{max}}{2} + 1 \right)^c - 1} \right) \qquad \forall \, 1 \le k \le \frac{k_{max}}{2} + 1$$

and $\quad Z_k = -Z_{k_{max} - k + 1} \qquad\qquad\qquad \forall \, \frac{k_{max}}{2} + 2 \le k \le k_{max}$

Here $a = 0.5$, $b = c = 0.3$, $X_{min} = X_1 = -70 R_E$, $X_{max} = X_{101} = +10 R_E$,

$Y_{min} = Y_1 = -25 R_E$, $Y_{max} = Y_{101} = +25 R_E$, $Z_{min} = Z_1 = -30 R_E$ and $Z_{max} = Z_{101} = +30 R_E$.

Changing a, b and c changes the spacing between the points in the grid. The indices i, j and k are set to be integer variables in the code.

The simulation code performs the trajectory tracing in two basic steps. In the first step it specifies the electric and magnetic field distributions over the magnetospheric grid, i.e. it computes the field values at every grid point. This is done for a variety of geophysical conditions, corresponding to 3 levels of magnetic storm activity and 24 cases of IMF. The models used to compute the fields and the selection of these parameters are discussed in detail in Sections 2.3 and 2.4.1, respectively. In the second step the code solves the equation of motion based on the initial conditions of the particles. As explained in Section 2.4.2, these are based on existing studies in the literature. Using the pre-computed field values over the grid, the solution to the equation of motion is obtained in the guiding center approximation by direct integration through a fifth-order Runge-Kutta algorithm with a variable step size [*Press et al.* 1992] as implemented in FORTRAN 90 (RKSUITE_90) by *Brankin et al.* [1995]. The trajectory results are used to derive the source and destination distributions for the ions (Chapter 3, Sections 3.2 to 3.4). The fraction of escaping particles (f) is defined to be the population of ions that is not gravitationally trapped or transported to the dayside. The destination distributions for the different geomagnetic conditions are then used to calculate the fraction of helium escape and the corresponding escape flux (Chapter 3, Sections 3.5 and 3.6).

2.2 Equation of motion

The trajectory of a particle is defined in terms of the evolution of its spatial coordinates with time. These coordinates at each point along the trajectory are obtained by solving the equation of motion of the particle at selected time intervals. While a plasma is

macroscopically electrically neutral, at the microscopic level, the individual ions are affected by the surrounding electromagnetic fields. In this section we look at how charged particles behave under the influence of electromagnetic fields near the Earth. The near-Earth plasma populations are extremely rarefied, and we can therefore treat the plasma as a collection of single particles, and analyze the motion of each individual particle separately.

The general equation of motion of a particle of mass m, charge q and velocity $\vec{v}$ under the influence of a combination of electric and magnetic fields $\vec{E}$ and $\vec{B}$ and a gravitational field $\vec{g}$ is

$$(2.2) \quad m\frac{d\vec{v}}{dt} = q\left(\vec{E} + \vec{v} \times \vec{B}\right) + m\vec{g}$$

In equation (2.2), the term $\vec{g}$ is acceleration due to gravity. Before we present the guiding center formulation of *Northrop* [1963] in Section 2.2.3 below, it is instructive to examine the properties of the equation of motion (2.2) in the special case of uniform magnetic field, and crossed electric and magnetic fields, respectively.

2.2.1 Uniform Magnetic Field

In the simple configuration of a pure magnetic field that is uniform in space and time, the solution to the particle equation of motion represents circular motion of a particle around the magnetic field. The component of the particle velocity parallel to the field ($v_{\parallel}$) is unaffected, and the direction of the particle's gyration is determined by the sign of its

charge q. A particle with non-zero $v_{||}$ traverses a helical path about the field line. This motion can be viewed as a superposition of two motions. The first is the circular motion (with gyroradius $r_g = m v_\perp / qB$; also known as Larmour radius) in the plane perpendicular to the field line, and the second is the motion parallel to the field line. This latter motion directed along the field line is called the guiding center motion and is a simplified description of the particle's path. The gyromotion around the guiding center can be neglected over large distances like those encountered while tracing particle trajectories around the Earth. This is known as the adiabatic approximation. The approximation is valid while the magnetic field does not change significantly over the scale of a gyroperiod.

2.2.2 Crossed Fields

Crossed electric and magnetic fields are often present in the high latitude ionosphere. The effect of the electric field is to make the guiding center drift across the magnetic field lines. In the case of a general force $\vec{F}$

$$(2.3) \quad m \frac{d\vec{v}}{dt} = \vec{F} + q(\vec{v} \times \vec{B})$$

This equation describes the gyration of the particle about its guiding center similar to that in a uniform magnetic field, with an additional drift of the guiding center that is given by

$$(2.4) \quad \vec{v}_d = \frac{\vec{F} \times \vec{B}}{qB^2}$$

Now, substituting the electric field as $\vec{F} = q\vec{E}$

$$(2.5) \quad \vec{v}_{\vec{E}\times\vec{B}} = \frac{\vec{E}\times\vec{B}}{B^2}$$

This is referred to as the $\vec{E}\times\vec{B}$ drift velocity and $\vec{v}_d$ is referred to as $\vec{v}_{\vec{E}\times\vec{B}}$. This drift is

independent of charge and all particles in crossed electric and magnetic fields experience

the same drift velocity.

In the case of a non-uniform magnetic field, the general form of a magnetic gradient force

is given by

$$(2.6) \quad \vec{F}_\nabla = -\mu\nabla\vec{B}$$

Here μ is the magnetic moment of a current loop that the gyrating ion can be equated to,

and is given by

$$(2.7) \quad \mu = \frac{mv_\perp^2}{2B}$$

It is known as the first adiabatic invariant and is a constant of the motion in the adiabatic

approximation of slowly varying fields. The requirement for μ to stay constant gives rise

to a process called magnetic mirroring in the Earth's dipole field. As a consequence of

the increase in magnetic field strength in the downward direction, there is an increase in

the perpendicular energy $\frac{1}{2}mv_\perp^2$ of a particle as the particle travels downward. This

comes at the expense of its parallel energy until the particle finally reverses direction and

starts to move upward, i.e. in the direction of decreasing $\vec{B}$. The force associated with the

mirroring is called the magnetic mirror force. Substituting the general form of this force

from equation (2.6) into the expression for drift velocity in equation (2.4) gives the drift

$$(2.8) \quad \vec{v}_\nabla = \frac{\mu}{qB^2} \vec{B} \times \nabla \vec{B}$$

There are a number of other guiding center drifts that arise from various field configurations that are not included here. The guiding center motion of a particle can be described in terms of a superposition of all the different drifts. However rather than deriving each drift separately, Section 2.2.3 presents a more general method.

2.2.3 Guiding Center Formulation

This formulation is taken from *Northrop* [1963]. If $\vec{r}$ is the instantaneous position of a particle under consideration and $\vec{R}$ is the position of the guiding center, the vector between them is $\vec{\delta} = \vec{r} - \vec{R}$, as shown in Figure 2.1.
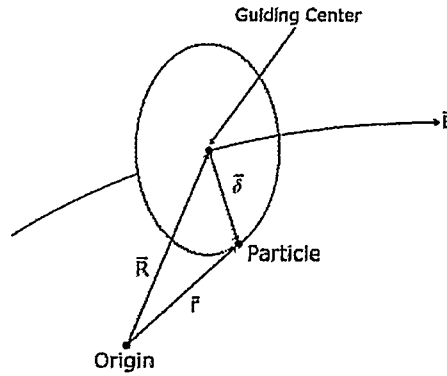
Figure 2.1. Motion of the guiding center.

The original equation of motion (2.2) may be written in terms of the guiding center position as

$$(2.9) \quad m(\ddot{\vec{R}} + \ddot{\vec{\delta}}) = q[\vec{E} + (\dot{\vec{R}} + \dot{\vec{\delta}}) \times \vec{B}] + m\vec{g}$$

We require the fields at the position of the particle so we perform Taylor expansions about the guiding center. Substituting $\vec{E}(\vec{r}) = \vec{E}(\vec{R}) + (\vec{\delta} \cdot \nabla)\vec{E}(\vec{R})$ and

$\vec{B}(\vec{r}) = \vec{B}(\vec{R}) + (\vec{\delta} \cdot \nabla)\vec{B}(\vec{R})$ into the equation of motion gives

$$(2.10) \quad \ddot{\vec{R}} + \ddot{\vec{\delta}} = \frac{q}{m}\left(\vec{E}(\vec{R}) + (\vec{\delta} \cdot \nabla)\vec{E}(\vec{R}) + (\dot{\vec{R}} + \dot{\vec{\delta}}) \times [\vec{B}(\vec{R}) + (\vec{\delta} \cdot \nabla)\vec{B}(\vec{R})]\right) + \vec{g}(\vec{R})$$

By defining three orthogonal coordinate system unit vectors $\hat{e}_1 = \hat{B}$, $\hat{e}_2$ perpendicular to the line of force, and $\hat{e}_3 = \hat{e}_1 \times \hat{e}_2$, $\vec{\delta}$ is expressed in terms of the basis vectors as

$\vec{\delta} = \delta(\hat{e}_2 \sin\theta + \hat{e}_3 \cos\theta)$ where $\theta = \int \omega_g dt$ is measured about the guiding center, ω_g being the gyrofrequency. Deriving the expressions for $\dot{\vec{\delta}}$ and $\ddot{\vec{\delta}}$ and calculating the time averages (assuming that coefficients such as $(\delta\hat{e}_2)$ are constant) gives $<\vec{\delta}> = <\dot{\vec{\delta}}> = <\ddot{\vec{\delta}}> = 0$. The time averaging of (2.10) over one gyroperiod, followed by a simplification of the equation using $\nabla \cdot \vec{B} = 0$ then yields

$$(2.11) \quad \ddot{\vec{R}} = \frac{q}{m}[\vec{E}(\vec{R}) + \dot{\vec{R}} \times \vec{B}(\vec{R})] - \frac{\mu}{m}\nabla B(\vec{R}) + \vec{g}(\vec{R}) + O(\varepsilon)$$

where ε is called the smallness parameter, and is a measure of the validity of the adiabatic approximation. Equation (2.11) is the equation of motion for the guiding center. Dotting and crossing this vector equation with $\hat{e}_1$, respectively give the parallel and perpendicular components

$$(2.12a) \quad m\frac{dv_\parallel}{dt} = mg_\parallel + qE_\parallel - \mu\nabla_\parallel B + m\vec{v}_{\vec{E}\times\vec{B}} \cdot \frac{d\hat{B}}{dt} + O(\varepsilon^2)$$

$$(2.12b) \quad \vec{v}_\perp = \frac{\vec{E}\times\vec{B}}{B^2} + \frac{\mu}{qB^2}\vec{B}\times\nabla B + \frac{m}{qB^2}\left[\vec{g} - \left(v_\parallel\frac{d\hat{B}}{dt} + \frac{d\vec{v}_{\vec{E}\times\vec{B}}}{dt}\right)\right]\times\vec{B} + O(\varepsilon^2)$$

Here the total time derivatives are convective derivatives

(2.13) $\quad \dfrac{d}{dt} \equiv \dfrac{\partial}{\partial t} + v_{\parallel}\nabla_{\parallel} + (\vec{v}_{\bar{E}\times\bar{B}} \cdot \nabla)$

The third term in equation (2.12a) is the magnetic gradient force. The fourth term

represents the centrifugal acceleration of the guiding center along the magnetic field. The

importance of this effect on ion transport was first demonstrated by *Cladis* [1986]. The

first term in equation (2.12b) is the ' $\vec{E} \times \vec{B}$ ' drift. The second term is referred to as the

'gradient B' drift, and the last three terms together constitute the 'acceleration drift'.

2.3 Fields

2.3.1 Magnetic Field

As mentioned before in Section 2.1.2, we use a combination of two models to specify the

magnetic field over the magnetospheric grid. The first is the IGRF model, which

calculates the contribution from the Earth's internal magnetic field. It is an empirical

representation of the Earth's field. The model represents the main (core) field without

external sources. The model employs a spherical harmonics expansion of the scalar

potential Ψ in geocentric coordinates, given by

(2.14) $\quad \Psi(r,\theta,\lambda_L,t) = K_{\Psi}R_E \displaystyle\sum_{n=1}^{N}\left(\dfrac{R_E}{r}\right)^{n+1}\sum_{m=0}^{n}(g_n^m(t)\cos(m\lambda_L)+h_n^m(t)\sin(m\lambda_L))P_n^m(\theta)$

where r is the radial distance from the Earth's center, θ is the colatitude, λ_L is the

longitude, K_{Ψ} is a constant of appropriate dimension, N is the maximum degree of the

expansion, $g_n^m(t)$ and $h_n^m(t)$ are the coefficients at time t and $P_n^m(\theta)$ are Schmidt semi-normalized associated Legendre functions of degree n and order m. The IGRF model coefficients are derived based on data sources including geomagnetic measurements from observatories, ships, aircraft and satellites. Given the year, day of the year, universal time and geographic coordinates of the point of interest, the model computes the desired magnetic field at the specified location in space.

Up to about 4 R_E, the contribution to the magnetic field is predominantly due to the Earth's core. Beyond that, influences from external sources created by solar wind interactions in the magnetosphere are increasingly dominant. The T96 model takes into account contributions from several external fields due to magnetospheric current systems including the ring current, magnetotail currents, magnetopause currents and large-scale field-aligned currents. It is a semi-empirical, best-fit representation based on a large number of satellite magnetometer observations. The field is modified with respect to several parameters which constitute the input to the model. These include the solar wind pressure, Dst index (this is a geomagnetic index which monitors the severity of magnetic storms by measuring fluctuations in the currents near the Earth), Y and Z components of the IMF and the dipole tilt angle. The tilt angle is the angle between the GSM Z-axis and the magnetic dipole axis. It is set by the input date and universal time, which we set to be January 1st, 00:30 UT. The rest of the input data sets are discussed in Section 2.4.1. The output from the T96 model is the magnetic field computed at a specified location in space.

2.3.2 Electric Field

2.3.2.1 Convection Electric Field

The solar wind is believed to induce electric fields in the magnetosphere and large scale

plasma convection near the Earth through a process called magnetic reconnection

[*Baumjohann and Treumann* 1997]. The nature of the reconnection depends on the

direction of the IMF. For southward IMF, solar wind magnetic field lines merge with the

Earth's dipole field lines on the dayside. The solar wind sweeps this connection anti-

sunward over the poles from the dayside towards the magnetotail. Here the lines

reconnect to form a closed terrestrial field line and a new solar wind field line. The

ionospheric plasma gyrating along the field lines follows the anti-sunward motion across

the polar cap. On magnetotail reconnection, the terrestrial field lines approach the Earth

and cross over to the dayside at lower latitudes, thereby replenishing the plasma to the

dayside before the entire process starts again.

For northward IMF, anti-parallel reconnection occurs on the anti-sunward side of the

Earth, inducing a different convection pattern. There is sunward convection over the

poles and return flow at slightly lower latitudes, down to 80°. At further lower latitudes,

there is a weaker form of the convection pattern seen for southward IMF conditions.

Eastward (dawn to dusk) orientations of the IMF cause the patterns to turn towards the

dawn (dusk) side over the northern (southern) hemisphere and this trend is reversed for

westward (dusk to dawn) orientations. These effects can be seen in Figure 2.2, which

depicts the statistical convection patterns. The patterns constitute the RG05 [*Ruohoniemi and Greenwald* 2005] model which is discussed in Section 2.3.2.3.

The plasma convection perpendicular to the magnetic field is associated with a corresponding convection electric field with higher potentials on the dawn side so that the field is generally directed towards dusk. This results in the ionospheric particles in the region always being under the influence of crossed electric and magnetic fields. The particles acquire an $\vec{E} \times \vec{B}$ drift as explained in Section 2.2.2. The motion of the drifting plasma traces equipotential lines over the high latitude region of the Earth. These potential patterns map along geomagnetic field lines with little attenuation [see eg. *Shepherd and Ruohoniemi* 2000]. The magnetospheric spatial grid where the particle traces are performed spans an altitude region where the parallel electric fields are negligibly small compared to the perpendicular electric fields ($E_{\parallel} < 10^{-7} Vm^{-1} << E_{\perp}$) and the assumption can be made [*Howarth and Yau* 2008] that the ionospheric potentials are projected to the magnetosphere with no attenuation. Tracing the Earth's magnetic field lines, the model calculates the potential at grid points located at higher altitudes in the magnetosphere based on the ionospheric potential value at the footprint of the field line near the Earth. Potentials and fields at points along a particle trajectory are interpolated from the values on the grid.

The potential patterns used as input were created using a statistical model developed at JHU APL. The model was developed based on six years of data from the Super Dual

Auoral Radar Network (SuperDARN) [*Greenwald et al.* 1995]. The potential maps are discussed in the next section.

2.3.2.2 Potential Maps

The network of SuperDARN radars provides measurements of convection velocity by observing the drift of ionospheric irregularities [*Ruohoniemi et al.* 1987]. The radars make the measurements by sending high frequency electromagnetic pulses into the ionosphere and measuring the Doppler shifted backscatter signal. Since each radar measures its line of sight component of the drift velocity, the radars operate in pairs and the two-dimensional $\vec{E} \times \vec{B}$ velocity is resolved by combining measurements from the common-volume area. There are currently 14 radars in the northern hemisphere and 7 in the southern hemisphere. The solution for the distribution of electrostatic potential can be determined by using the radar measurements as shown by *Ruohoniemi and Greenwald* [1996]. The convection electric field is related to the potential distribution by $\vec{E} = -\nabla\Phi$ and Φ can be expresses as a series in spherical harmonics as follows

$$(2.15) \quad \Phi(\theta, \phi) = \sum_{l=0}^{L} A_{l0} P_l^0(\cos\theta) + \sum_{m=1}^{l} (A_{lm} \cos m\phi + B_{lm} \sin m\phi) P_l^m(\cos\theta)$$

Here P_l^m are the associated Legendre polynomials, and A_{lm} and B_{lm} are real-valued coefficients which are determined by minimizing the quantity $\sum_i |E_i - \nabla\Phi|^2$ where $\vec{E} = -\vec{v} \times \vec{B}$. Large-scale convection maps can be derived based on all the available velocity data [*Ruohoniemi and Baker* 1998]. As the radar array does not yet have global

coverage and the radars do not operate at all times, there are regions and times where no real velocity measurements exist. The statistical JHU APL model provides electric potential information for periods and regions that might not be available in the real data. The convection patterns are parameterized by the magnitude and direction of IMF in the GSM Y-Z plane. The output is in the form of maps that display the potential variation over the polar regions over a latitude-longitude grid spaced one degree in latitude and two degrees in longitude apart. The maps can be fitted to real SuperDARN measurements for specific times, or can be used in the purely modeled form based on input IMF conditions. We use the latter method in this study.

2.3.2.3 The RG05 Convection Model

In a basic characterization of the IMF dependencies of the convection, the RG05 convection model [*Ruohoniemi and Greenwald* 2005] consists of 24 patterns, binned by IMF magnitude and clock angle in the GSM Y-Z plane. The 3 magnitude ranges considered are 0–3, 3–5 and 5–10 nT, respectively. The 8 IMF orientations are indicated in Figure 2.2, which displays the convection maps for the IMF magnitude range 0–5 nT.

Ruohoniemi and Greenwald [1996] developed a one-radar model which described the IMF dependencies by considering the three magnitude ranges 0–4, 4–6 and 6–12 nT, and the same 8 IMF orientations. The RG05 model improves on the earlier model by analyzing the database of nine radars that were in operation at the time in the northern hemisphere, using measurements collected over the period 1998-2002. The change in the

binning of IMF magnitude was made to balance the IMF occurrence statistics more

evenly.
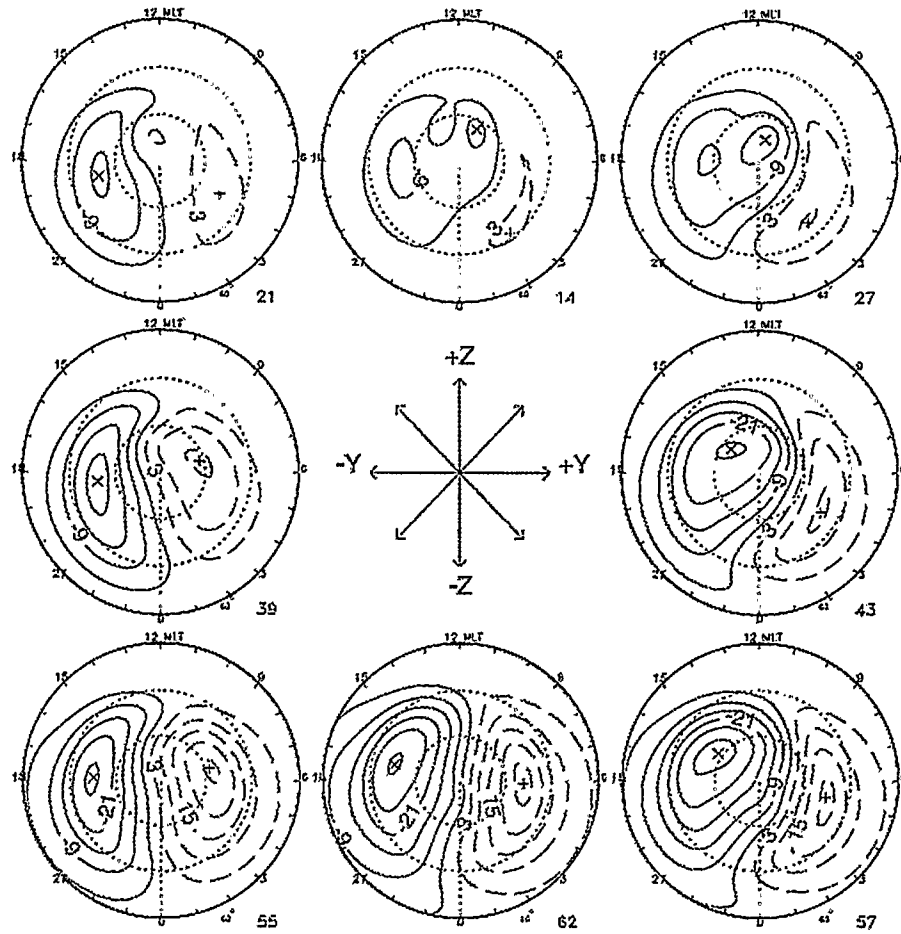
Figure 2.2. Statistical convection patterns sorted by IMF direction in the GSM *Y-Z* plane for the IMF magnitude interval 5–10 nT. [Taken from *Ruohoniemi and Greenwald* 2005]

Figure 2.2 shows that the two-cell pattern expands significantly for southward IMF in

comparison with northward IMF, a result of increased reconnection between the field

lines as discussed earlier in this section. The pattern is also intensified for increased

magnitude of southward IMF. The dawn and dusk cells are sculpted into more rounded or

crescent shapes depending on the sign of B_Y. Finally, values for the cross polar cap

potential are consistently higher for B$_Z$ negative versus B$_Z$ positive, and for B$_Y$ positive versus B$_Y$ negative.

2.3.3 Gravitational Field

The gravitational acceleration experienced by the particles is computed using Newton's gravitation formula, in the approximation that the Earth is perfectly spherical.

$$(2.16) \quad \vec{g} = \frac{-GM_E}{r^2}\hat{r}$$

Here M_E is the Earth's mass, r is the geocentric distance of the particle and G is the universal gravitation constant.

2.4 Input Data Sets

2.4.1 Field Models

The T96 model requires as input the solar wind dynamic pressure P_{dyn}, given by

$$(2.17) \quad P_{dyn} = m_i n_{sw} v_{sw}^2$$

where m_i is the proton mass, n_{sw} is the solar wind density and v_{sw} is the bulk velocity. The measurements of these parameters were taken from the Solar Wind Electron Proton Alpha Monitor (SWEPAM) on ACE (Advance Composition Explorer). We compiled the occurrence statistics and average P_{dyn} values for two years, one each at solar minimum

(2006) and solar maximum (2000). Based on the distributions shown in Figure 2.3(a), P_{dyn} was set at 2 nPa and kept the same throughout the entire simulation.
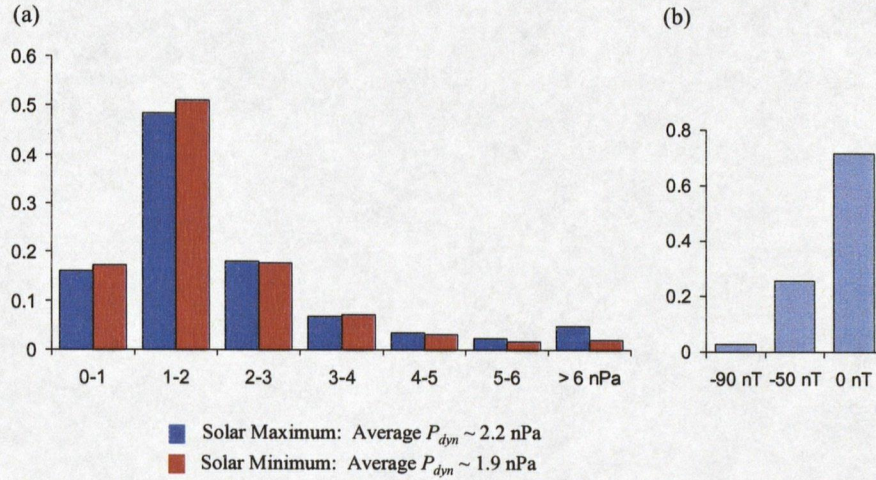
Figure 2.3. Occurrence distributions for (a) P_{dyn} at two years, one each at solar maximum and solar minimum, and (b) Dst.

We also compiled the occurrence statistics for the Dst (defined in Section 2.3.1) values for a year each at solar minimum and maximum. The distributions for the two years have been combined in Figure 2.3(b). Magnetically quiet times (or lower absolute Dst values) are significantly more common than times of higher magnetic storm activity. Since for an accurate estimation of global helium escape we need to be able to describe the outflow over a range of geomagnetic conditions, we have selected the three Dst values of 0, –50 and –90 nT as input to the model for magnetically quiet, moderate and storm times, respectively.

The IMF input to the model serves two purposes. It modifies the external field from the T96 model and also parameterizes the RG05 input electric potential maps (described in

Section 2.3.2.3). IMF data from magnetometers on IMP-8 (Interplanetary Monitoring

Platform) for two years, one each at solar minimum and maximum showed a fairly

uniform occurrence distribution in the $+Z$, $-Z$, $+Y$ and $-Y$ directions. As discussed

previously in Section 2.3.2.3, the RG05 electric potential model [*Ruohoniemi and*

Greenwald 2005] is divided by 3 main ranges of IMF magnitude in the GSM Y-Z plane,

namely 0–3, 3–5 and 5–10 nT, respectively. Based on this, we have selected three values

of IMF magnitude at 1.5, 4 and 7.5 nT in this study to represent the same 3 IMF

magnitude ranges, and then divided each into 8 directions in the GSM Y-Z plane. These

constitute the 24 cases of IMF for each of the Dst values. The data sets used for the Dst,

IMF and P_{dyn} analysis were downloaded from the online resources of CDAWeb[4] and

OMNIWeb[5] at NASA Goddard Space Flight Center.

2.4.2 Initial Particle Conditions

The initial positions of the particles are distributed uniformly above ILAT ~ 70° at

altitude 7,000 km. The initial velocities are selected using a drifting Maxwellian

distribution (based on T, $v_{\perp}, v_{\parallel}$). In Chapter 1 (Section 1.2) we discussed the ion

temperature which lies roughly between 0.05 to 0.35 eV [*Drakou et al.* 1997]. In this

study we initially set the temperature to 0.1 eV, and later performed another set of

simulations at the higher temperature of 0.2 eV to investigate the temperature dependence

---

[4] http://cdaweb.gsfc.nasa.gov/ as of July 2009

[5] http://omniweb.gsfc.nasa.gov/ as of July 2009

of the escape fraction. The perpendicular component of the initial velocities is calculated

from the $\vec{E} \times \vec{B}$ drift at each point. The parallel component is set based on the helium

velocity map shown in Figure 2.4, which is divided into two bulk velocity cases indicated

as 'Lower' and 'Higher'. This was adapted from the map of *Abe et al*. [1993] (Chapter 1,

Figure 1.6). A drifting Maxwellian distribution based on the lower (higher) bulk velocity

results in the particles having a lower (higher) initial energy distribution. Consequently, a

smaller (larger) fraction of ions is able to escape the atmosphere, since a particle's initial

energy strongly influences its trajectory and ability to escape the Earth's atmosphere.

Therefore, the two bulk velocity limits correspond to limits on the ultimate fraction of

escape.

Bulk velocity limits (km/s)

	Lower	Higher
	6	9
	2	4
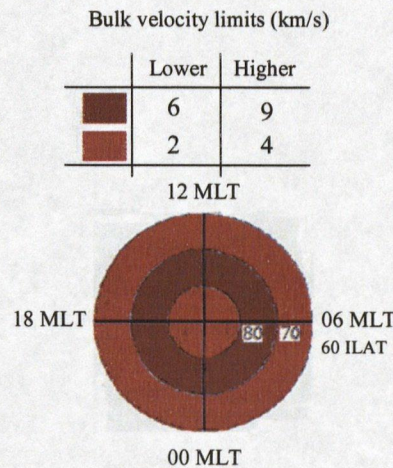
Figure 2.4. Polar plot of averaged parallel ion velocity as a function of invariant latitude and magnetic local time, adapted from velocity map presented by *Abe et al.* [1993].

Chapter Three: Results

3.1 Simulations

The previous chapter detailed the input to the model (Section 2.4). Table 3.1 summarizes how we organized the simulations. We traced 40,000 particles for each of the cases listed. The total number of simulation sets was therefore 2 (bulk velocity maps) × (3+1) (Dst-temperature combinations) × 24 (IMF).

Temperature	Bulk Velocity	Dst	IMF
0.1 eV	*2 cases* Lower Higher	*3 cases* 0 , −50 and −90 nT	*24 cases* 3 magnitude ranges (1.5 , 4 and 7.5 nT) × 8 directions in the GSM *Y-Z* plane
0.2 eV	*2 cases* Lower Higher	*1 case* 0 nT	*24 cases as above*

Table 3.1. Organization of the temperature, bulk velocity, Dst and IMF cases for particle tracing simulations.

Since the guiding center paradigm is valid only under adiabatic conditions, particle tracing is stopped for trajectories that enter regions in the magnetosphere where ions can become non-adiabatic. There are a number of conditions under which tracing is stopped. These are the same as those used by *Howarth and Yau* [2008] and are listed below. *Cully*

[2001] and *Cully et al.* [2003b] stopped trajectory traces for a similar set of conditions and the comparison is also included here.

1. An ion is gravitationally trapped. An ion is considered trapped if its altitude after 2 hours of flight is below 1 R_E (below 2 R_E in *Cully* [2001]) or it reaches an altitude below 600 km at any point.

2. An ion flows to the distant tail of the magnetosphere and out of the tracing region, i.e. beyond 70 R_E in the negative GSM X direction, or $\pm$ 25 R_E and $\pm$ 30 R_E in the GSM Y and Z directions, respectively. The fraction of ions in this category is very small, lying <5% for all simulation cases. (Particles were stopped if they crossed the plane at $X = -60$ R_E in *Cully* [2001].)

3. An ion hits the magnetopause, which is defined by the T96 model. (The magnetopause was defined to be the envelope of field lines traced from the Earth in *Cully* [2001].)

4. An ion crosses the dayside equatorial plane. (Particles were stopped if they crossed any point on the equatorial plane in *Cully* [2001].)

5. An ion crosses the Plasma Sheet Boundary Layer (PSBL). The magnetic field lines are highly curved in this region and the ions behave non-adiabatically. Similar to *Howarth and Yau* [2008], the layer is defined as a linear function of the dipole tilt angle by $Z_{GSM} = (4.96\theta_{tilt} + 4)R_E$ for $X_{GSM} < -15R_E$ and $Z_{GSM} = (-0.38\theta_{tilt} - 0.2)X_{GSM}$ for $X_{GSM} \geq -15R_E$,

where θ_{tilt} is measured in degrees. (*Cully* [2001] stopped the particles

when they entered the central plasma sheet, the upper boundary of which

was defined to be at $Z = 3R_E$ for $X < -15R_E$ and the plane

$Z = (X/7.5+1)R_E$ inside $X = -15R_E$.)

Cully [2001] also monitored the adiabatic behaviour of the particles, and stopped tracing

particles if they were deemed to be non-adiabatic, i.e. if they satisfy the condition of

$\sqrt{R_c/R_{Lmax}} < 3$ [*Delcourt and Belmont* 1998], where R_c and R_{Lmax} are the minimum field

line curvature encountered by a particle in a given time step, and the maximum Larmour

radius during that time step, respectively.

3.2 Single Ion Traces

We analyze the motion of a number of ions at different initial energies and under various

geomagnetic conditions. We consider six ions, one from each of six source regions:

dayside and nightside auroral zones, and noon, dusk, midnight and dawn polar cap zones.

Though the coordinates of the auroral oval and region of outflow vary with magnetic

activity [*Andersson et al.* 2004], the selection of source regions employed here does not

take that into account. We follow the selection made by *Howarth and Yau* [2008], as it is

convenient for the purpose of this study and for making comparisons with their results.

Defined explicitly in Figure 3.1, the six source regions are (1) *Lower latitude (LL) day*

(06 < MLT < 18; <75° ILAT), (2) *LL night* (18 < MLT < 06; <75° ILAT), (3) *Higher*

latitude (HL) day (09 < MLT < 15; >75° ILAT), (4) *HL dusk* (15 < MLT < 21; >75° ILAT), (5) *HL night* (21 < MLT < 03; >75° ILAT) and (6) *HL dawn* (03 < MLT < 09; >75° ILAT).
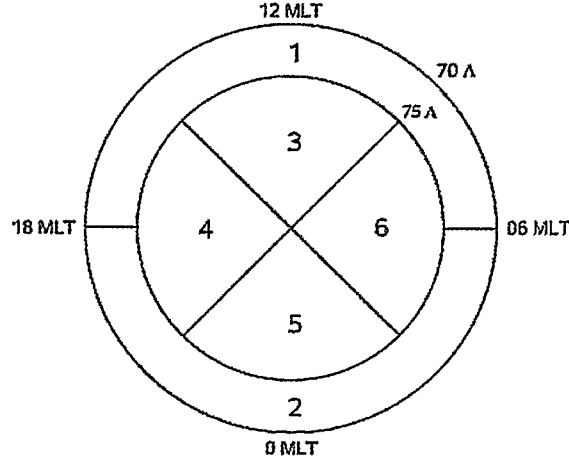
Figure 3.1. Source regions as a function of MLT and ILAT. [Taken from *Howarth and Yau* 2008]

Figures 3.2 and 3.3 depict the motion for the cases of Dst = 0 nT and Dst = –90 nT, respectively. Each of the figures is divided into the top left, top right, bottom left and bottom right quadrants, corresponding to traces at the four initial energies of (a) 0.1 eV, (b) 0.5 eV, (c) 1 eV and (d) 2 eV, respectively. Each quadrant is further subdivided into traces corresponding to conditions of southward and northward IMF in the left and right columns, respectively. The IMF magnitude in both cases is 7.5 nT. A stack of three plots representing Z_{GSM} (R_E) vs. X_{GSM} (R_E), Y_{GSM} (R_E) vs. X_{GSM} (R_E) and *Energy* (eV) vs. *Time* (s) is presented for each of the above cases.

First we consider the case of magnetically quiet conditions (Dst = 0; Figure 3.2). Figure 3.2(a) shows that in the lowest energy case (0.1 eV), all six particles are gravitationally

trapped for both IMF conditions. They have initial energies that are insufficient for them to escape. Figure 3.2(b) corresponds to the higher energy of 0.5 eV, and it shows that the particles are trapped under northward IMF conditions but are able to travel to further distances for southward IMF. This behaviour is expected because for southward IMF, the convection electric field is stronger, resulting in larger centrifugal acceleration, which provides the particles with enough energy to escape. The particle originating on the lower latitude night side travels the furthest distance from the Earth, with a trace time more than twice as long as any of the other particles. None of the particles are trapped for the cases of initial energy of 1 eV and 2 eV, which are shown in Figures 3.2(c) and 3.2(d), respectively.

In the energy versus time plots, the energy falls in the initial portion of a particle's trajectory. Any upward acceleration acting on the particle this early in the trace is exceeded by the gravitational pull it faces. The resulting reduction in energy occurs in the initial portion of all the traces for all four energies and is most clearly visible in cases (a) and (b) where the final energies are significantly lower than the other cases. In case (a) after approximately 20 minutes of flight, the ions start to accelerate. This continues until the trace is stopped when the particles are gravitationally trapped (this is one of the conditions listed in Section 3.1). The energy evolution of the particles traced under B_Z positive conditions in case (b) is similar. However, the energy evolution under B_Z negative conditions is different. The particles that are not trapped enter regions at higher altitudes where the magnetic field lines are more curved, causing an increase in energy due to larger centrifugal acceleration.
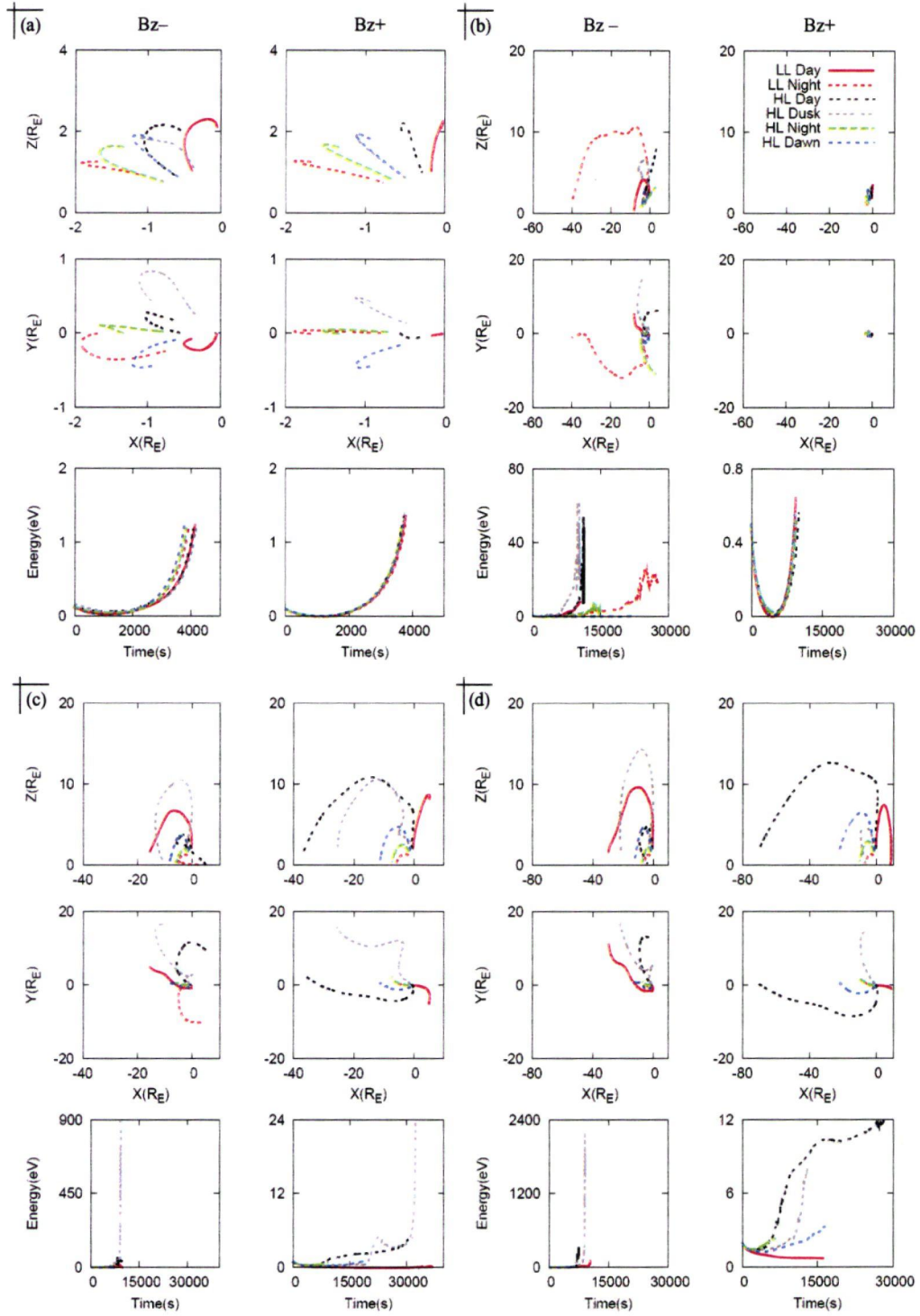
Figure 3.2. Trajectory and energy plots for 6 ions (one for each of the source regions shown in Figure 3.1: *LL day, LL night, HL day, HL dusk, HL night, HL dawn*) at **initial parallel energies of (a) 0.1eV , (b) 0.5eV , (c) 1eV and (d) 2eV, for southward and northward IMF (left and right column, respectively) at each energy. All cases are for Dst = 0nT.**

Examining the particles originating at *LL day* (lower latitude dayside) for cases (c) and

(d), we note that in both cases the ion travels to the nightside under B_z negative

conditions while it stays on the dayside for B_z positive conditions. This effect is in

agreement with the occurrence of higher ion convection under southward IMF conditions,

which would sweep the particle to the nightside. The particle originating at *HL day*

(higher latitude dayside) appears to reach a significantly larger distance downtail under

B_z positive conditions than under B_z negative, which is unexpected. We note, however,

that the trace time for the ion in both cases (c) and (d) is 3 to 4 times longer for the case

of northward versus southward IMF. The ion traces are stopped (as per the conditions

listed in Section 3.1) significantly earlier in the higher energy B_z negative cases. The ion

trajectories represented in Figure 3.2 have travel times that vary from 1 hour to over 10

hours, and a valid comparison of the traces is more complicated than a simple contrast of

the physical coordinates of the destination. The *HL dusk* particles in Figures 3.2(c) and

3.2(d) for B_z negative conditions reach energies typical of the plasma sheet, where

particles become non-adiabatic and undergo marked acceleration.

We examine Figure 3.3, which depicts the traces for high magnetic storm activity, and

compare the general characteristics of the ions to those exhibited in the magnetically

quiet cases in Figure 3.2. The effects of Dst in the case of the lowest initial energy (0.1

eV; Figures 3.2(a) and 3.3(a)) are insignificant. The ions are trapped and follow almost

identical trajectories in the two Dst cases. In the lower energy case, the ion energies are

too low for the ions to escape irrespective of the magnetic activity conditions. There is no
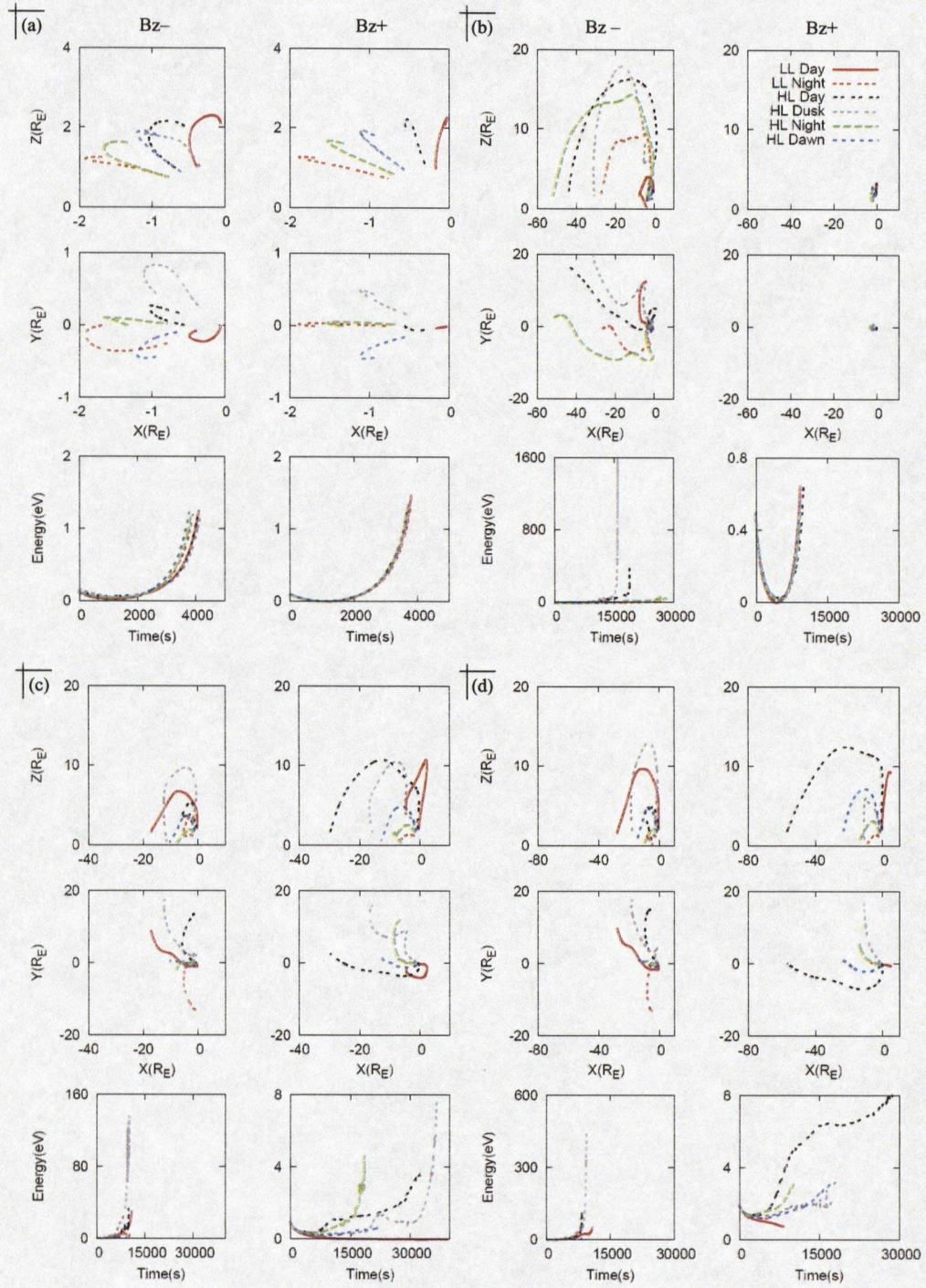
Figure 3.3. Trajectory and energy plots in the same format as Figure 3.2 but for conditions corresponding to Dst = −90nT.

marked difference in the trajectories for the higher initial energy cases of 1eV (Figures 3.2(c) and 3.3(c)) and 2 eV (Figures 3.2(d) and 3.3(d)) either. The ion energies are sufficient for them to be able to escape and again, Dst plays no significant role in the distances to which they are able to travel. The energy versus time plots show that the final energy of the highly accelerated *HL dusk* particle is higher for the Dst = 0 nT case, and up to 5 times higher for the case of B_Z negative at 2 eV.

The effect of Dst on the trajectories is most pronounced for the intermediate case of initial energy 0.5 eV (Figures 3.2(b) and 3.3(b)) under B_Z negative conditions. The ions travel much further away from the Earth under magnetically disturbed conditions (Dst = –90 nT). All the ions except the *LL day* particle travel to distances at least 30 R_E downtail. The highly energized *HL dusk* ion in this case achieves a much higher energy at storm time than at quiet time, which is the opposite behaviour to the higher energy B_Z negative *HL dusk* ions.

At the lowest energy of 0.1 eV, we also analyze the effect of initial pitch angle on the ion trajectories. Figure 3.4 shows the trajectories (Z_{GSM} (R_E) vs. X_{GSM} (R_E) and Y_{GSM} (R_E) vs. X_{GSM} (R_E)) for the six particles originating at (1) *LL day*, (2) *LL night*, (3) *HL day*, (4) *HL dusk*, (5) *HL night* and (6) *HL dawn*, stacked top to bottom, respectively. In each case, the two left and the two right panels show the *Z-X* and *Y-X* plots, respectively. The trajectories are shown for both B_Z negative and B_Z positive conditions. We have considered pitch angles between 180° and 105° at intervals of 15°. The particles are all gravitationally trapped. While the initial portions of the trajectories diverge because of
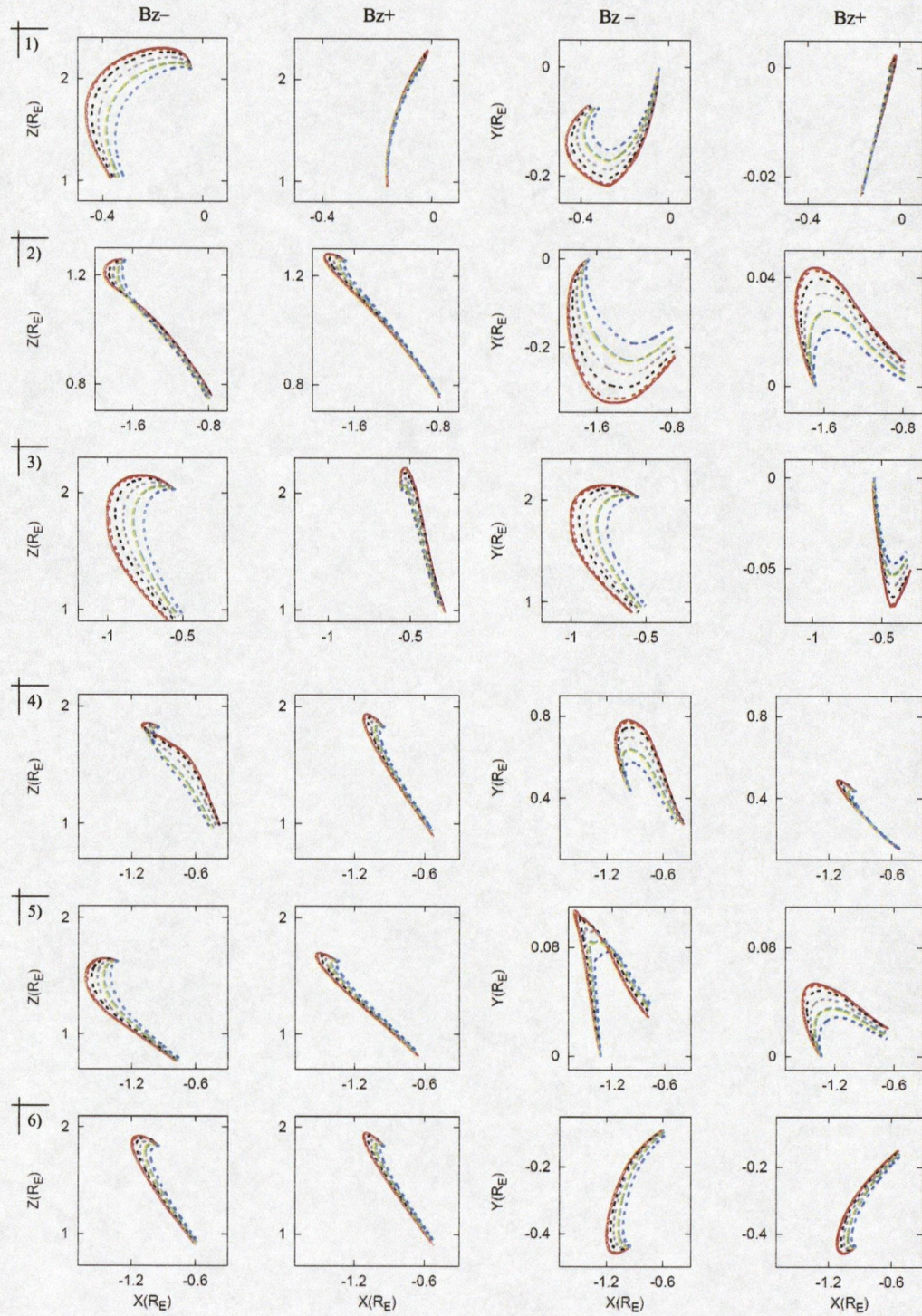
Figure 3.4. Trajectory plots for ions with total initial energy 0.1eV originating at (1) *LL day*, **(2)** *LL night*, **(3)** *HL day*, **(4)** *HL dusk*, **(5)** *HL night* **and (6)** *HL dawn*. **From each source region there are 6 ions with initial pitch angles varying between between 180° (red line) and 105° (blue line) at intervals of 15°.**

the difference in pitch angle, the trajectories merge back together before arriving at their final coordinates. Note that the data in different panels in this graph are in general displayed with different scales in order to make the effect of pitch angle on the trajectories more clearly discernible.

3.3 Destination Distributions sorted by IMF

The trajectory data was used to determine the destinations of the particles, by sorting the ions into eight categories based on the final coordinates of their trajectories. The first category is gravitationally trapped ions (GT in Figures 3.5 to 3.8), defined by the conditions stated in Section 3.1. The next three categories are those that flow to the distant tail (DT) beyond -70 R_E, hit the magnetopause (MP) or convect to the dayside (DS). The last four categories are for ions that hit regions in the plasma sheet, which is divided into four sectors, namely near-Earth dawn (PN), near-Earth dusk (PK), tail dawn (TN) and tail dusk (TK). The near-Earth regions are defined by $X_{GSM} > -15$ R_E while the tail regions are defined by $X_{GSM} < -15$ R_E. The dawn and dusk regions are defined by $Y_{GSM} < 0$ R_E and $Y_{GSM} > 0$ R_E, respectively.

Figures 3.5 and 3.6 show the helium ion distributions for the lower and higher bulk velocity cases, respectively. For each of these, we focus on four primary temperature-Dst cases. These are (a) T = 0.1 eV, Dst = 0 nT; (b) T = 0.1 eV, Dst = -50 nT; (c) T = 0.1 eV, Dst = -90 nT and (d) T = 0.2 eV, Dst = 0 nT. The distributions for the 8 orientations of IMF in the GSM Y-Z plane are displayed in both figures. The IMF direction vector is
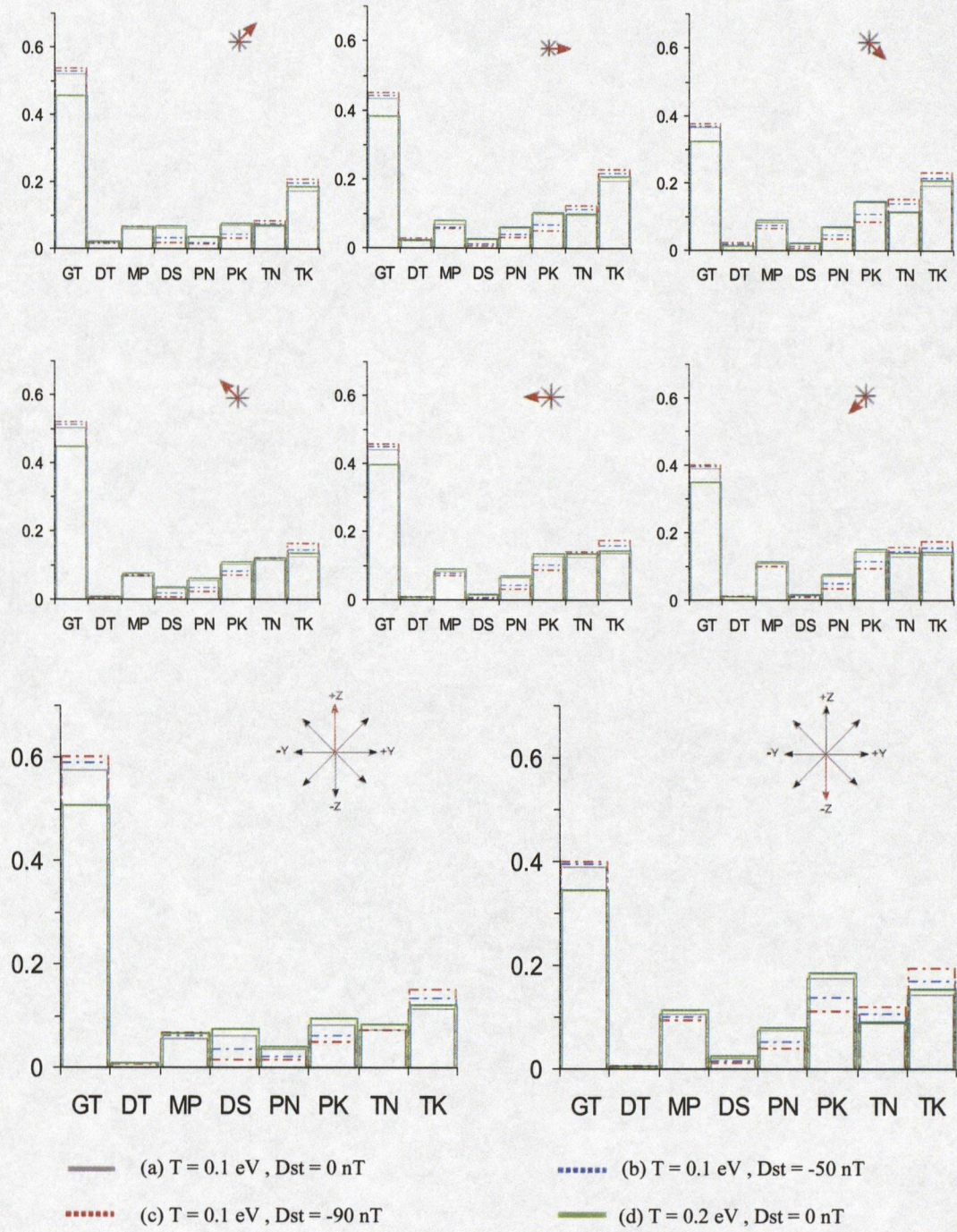
Figure 3.5. Destination distributions sorted by IMF direction for the four principal cases: (a) T = 0.1eV, Dst = 0nT; (b) T = 0.1eV, Dst = –50nT; (c) T = 0.1eV, Dst = –90nT; (d) T = 0.2eV, Dst = 0nT for the case of the lower bulk velocity.

indicated by the red arrow head next to each panel. The destination distributions corresponding to the 3 IMF magnitudes (1.5, 4 and 7.5 nT) were found to be qualitatively very similar for all IMF orientations and the data sets have been combined to produce the resultant distributions shown in Figures 3.5 and 3.6. The error bars associated with the graphs are negligibly small, and have been excluded.

The number of gravitationally trapped ions (GT) is significantly higher in the case of the lower bulk velocity (Figure 3.5). This is expected, because in the case of the higher bulk velocity, the ions have initial energies that are higher and more of them are therefore able to escape. The gravitationally trapped portion at the higher temperature of 0.2 eV (colour coded green) is consistently smaller under all the IMF conditions in both Figures 3.5 and 3.6. This is also expected, as the average initial energies are higher in this case. The difference is larger in the case of lower initial bulk velocities, where the larger spread in the Maxwellian distribution due to the higher temperature would play a more significant role in increasing the number of particles able to escape.

The trapped portion (GT) is also considerably lower for cases with southward versus northward IMF due to stronger magnetic reconnection and convection electric field, which cause larger centrifugal acceleration. This result is in agreement with the observations made by *Howarth and Yau* [2008] for O^+ ions. Our results pertaining to the fraction of ions that reaches the distant tail (DT; beyond 70 R_E downtail) are also consistent with effects reported in their work. They found that the fraction of H^+ and O^+ ions that travel that far was reduced for southward versus northward IMF due to a

(a) T = 0.1 eV , Dst = 0 nT
(b) T = 0.1 eV , Dst = -50 nT
(c) T = 0.1 eV , Dst = -90 nT
(d) T = 0.2 eV , Dst = 0 nT
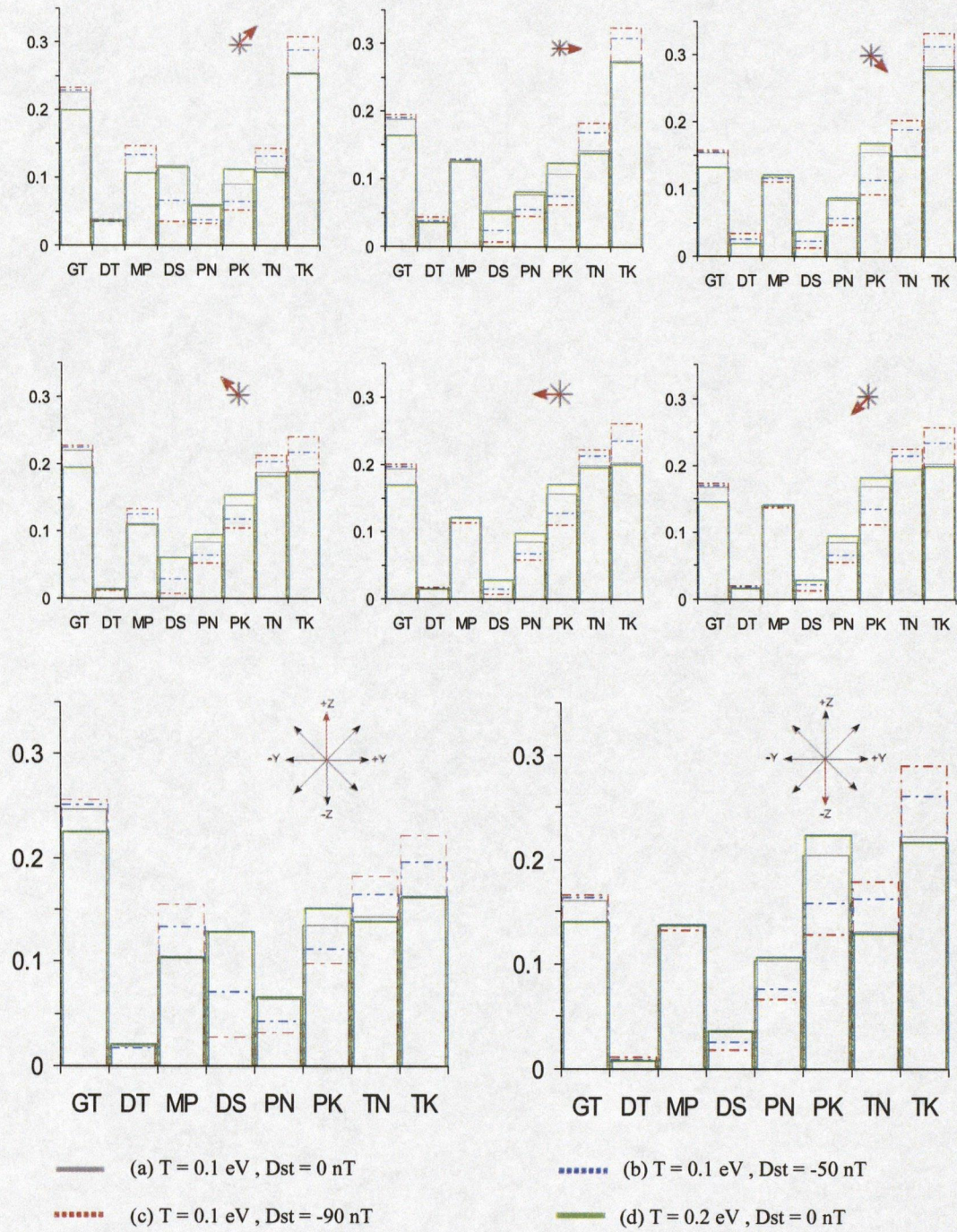
Figure 3.6. Same as Figure 3.5 but for the case of the higher bulk velocity.

stronger $\vec{E} \times \vec{B}$ drift caused by increased electric field. These effects agreed with earlier work by *Delcourt et al.* [1993, 1994], *Winglee* [2000] and *Cully et al.* [2003b]. We see the same behaviour with the He$^+$ ions in this study, even though the fraction that reaches the distant tail is small, lying below 5% for all the Dst and IMF cases.

The fraction of particles that convect to the dayside (DS) decreases with increasing magnetic storm activity. This is one of the few clear inferences that we are able to make about the effect of Dst. The effects are somewhat difficult to isolate, partly because they are varied for the different destinations and temperature cases, and the differences between the four temperature-Dst cases in Figures 3.5 and 3.6 with respect to the destination distributions are not significant.

We examine the number of particles reaching the plasma sheet (PS) in the lower temperature case. The portion of particles that reach the PS on the dusk side (PK + TK) is found to be consistently larger than that on the dawn side (PN + TN), with negligible dependence on Dst or IMF magnitude. On investigating the dependence of the IMF Y component, we find that the difference between PS dusk and dawn ions is higher for positive B$_Y$ conditions than negative B$_Y$ conditions. For the lower bulk velocity, the fraction of dusk PS particles is ~ 1.4 to 1.9 times the fraction of dawn PS particles, with the larger difference corresponding to times of positive B$_Y$. For the higher bulk velocity the ratio is ~ 1.3 to 1.8. *Howarth and Yau* [2008] made similar observations with H$^+$ and O$^+$ ions and attributed the results to the effect that the IMF B$_Y$ has on turning the convection pattern dawnwards when it is positive, thereby contributing a duskward

component to the $\vec{E} \times \vec{B}$ velocities of the ions and causing particle flow to favour the dusk side.

We observe that the fraction of PS ions reaching the tail region (TN + TK) is consistently higher than that reaching the near-Earth region (PN + PK). When the fractions are sorted by Dst and IMF strength, the ratio of tail ions over the near-Earth ions is found to increase with magnetic storm activity and decrease with IMF strength, implying that the PS distribution shifts tailwards for higher storm activity and lower IMF strength. For the lower bulk velocity, the ratio lies between ~ 1.3 (for quiet time Dst and strongest IMF) to ~ 3.3 (for storm time Dst and weakest IMF strength). For the higher bulk velocity, the ratios are both slightly larger, lying between ~ 1.5 to ~ 3.6. This shows that the higher velocities also contribute a tailward shift to the PS destination distribution.

3.4 Destination Distributions sorted by Source Region

In addition to categorizing the particles into different destination regions, we have also sorted them by the six source regions defined in Section 3.2 and Figure 3.1 (i.e. the dayside and nightside auroral zones, and the noon, dusk, midnight and dawn polar cap zones). Figures 3.7 and 3.8 show the destination distributions of ions from each source region. Data for all 24 IMF cases have been included in these two figures in order to elucidate the source dependence of the distributions. The gravitationally trapped fraction is higher for the *HL* source regions than for the *LL* regions. Averaged over Dst and IMF, the fraction of trapped ions (GT) originating in *HL* regions is ~ 2 and 8 times higher than

(1) LL Day (06 < MLT < 18 ; <75° ILAT)

(2) LL Night (18 < MLT < 06 ; <75° ILAT)

(3) HL Day (09 < MLT < 15 ; >75° ILAT)

(4) HL Dusk   (15 < MLT < 21 ; >75° ILAT)

(5) HL Night (21 < MLT < 03 ; >75° ILAT)

(6) HL Dawn (03 < MLT < 09 ; >75° ILAT)

(a) T = 0.1 eV , Dst = 0 nT

(b) T = 0.1 eV , Dst = -50 nT

(c) T = 0.1 eV , Dst = -90 nT

(d) T = 0.2 eV , Dst = 0 nT
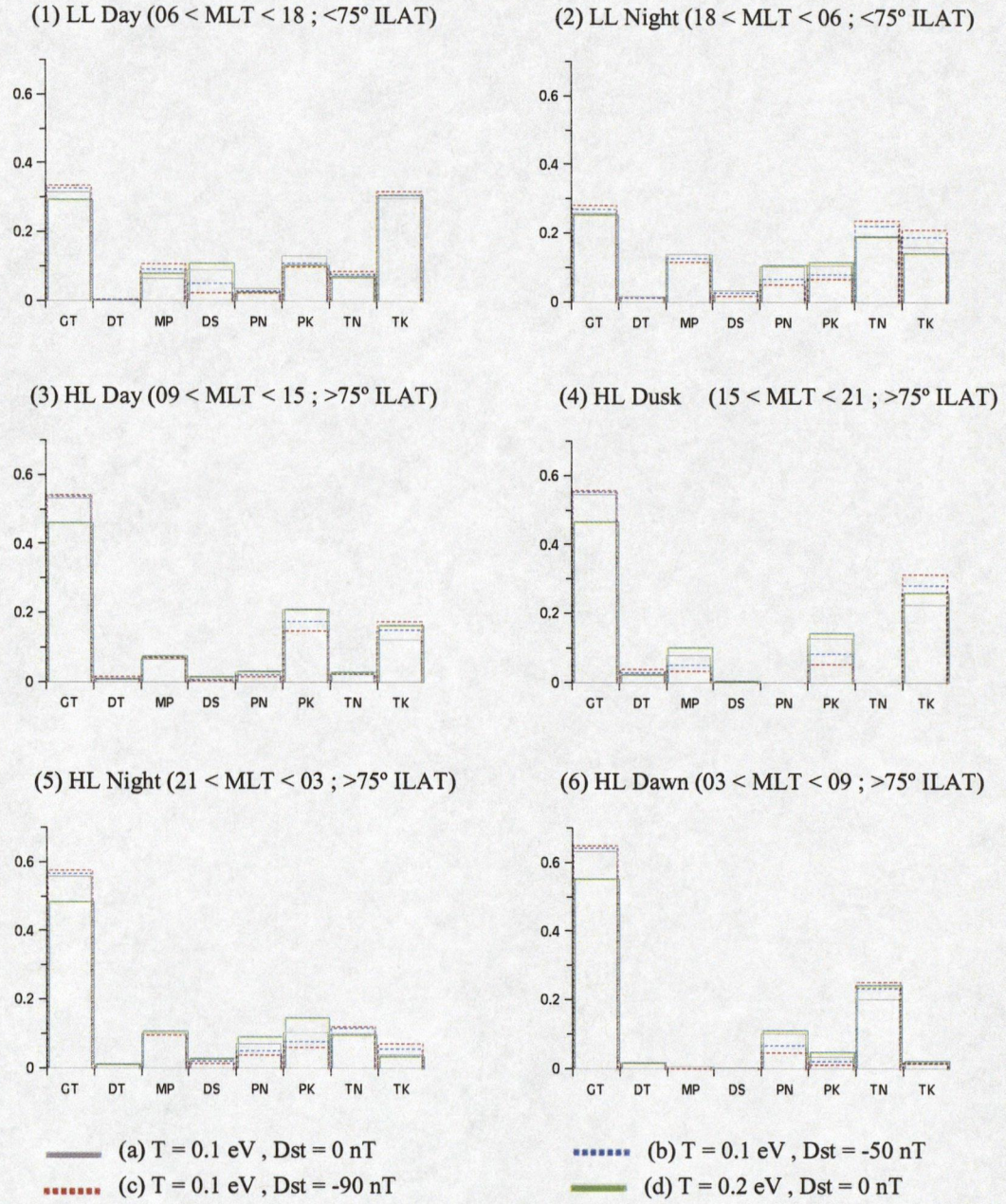
Figure 3.7. Destination distributions divided by source region for the case of lower bulk velocity (all acronyms used have been defined in the text.)

that originating in *LL* regions for the cases of lower and higher bulk velocity,

respectively. The portion that convects to the dayside (DS) appears to originate mostly

from the *LL* day region. Also, on average, particles originating on the day side that reach

the PS seem to favour the dusk side (PK + TK), while those originating on the night side
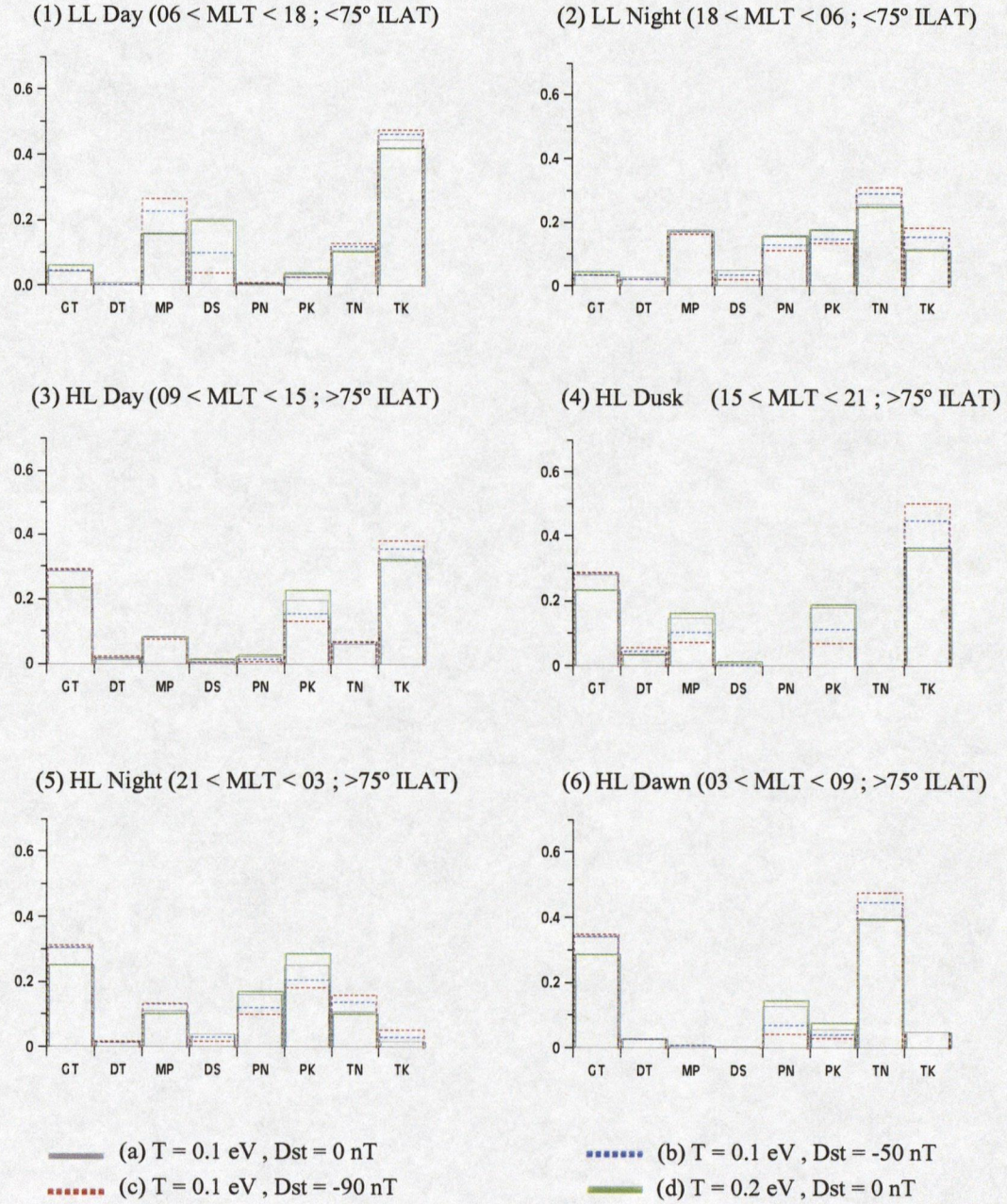
Figure 3.8. Same as Figure 3.7 but for the case of higher bulk velocity.

are more evenly distributed between the dusk and dawn sectors.

The fraction of He$^+$ ions starting in the dusk region that travel to the dawn side is negligible (<0.1% for all cases). The number of particles from the dawn side that reach the dusk side is larger, reaching ~ 7% for the lower bulk velocity case and ~ 13% for the higher bulk velocity case. In similar results, *Howarth and Yau* [2008] found that O$^+$ ions originating in the dusk sector were not transported outside the dusk sector, while ions originating in the dawn sector were generally able to escape to either side in the magnetosphere. The effect was attributed to the average dawnward rotation of the convection cell pattern.

3.5 Escape Fractions

In Chapter 2, Section 2.1.3, the escaping fraction (f) of helium ions was defined as the portion of ions that is not gravitationally trapped and has not convected to the dayside. Figures 3.9 and 3.10 show the escape fractions for our four principal temperature-Dst cases for the lower and higher bulk velocities, respectively. In each case, the fractions are sorted by IMF orientation and magnitude. In both figures, the 8 IMF directions are labelled on the top left panel, and the three IMF magnitudes are colour-coded. The corresponding escape fractions are printed next to each IMF direction. For example, in Figures 3.9(a) and 3.10(a), for northward (Z+) IMF, the escape fractions are ~ 37% and ~ 63% for the lower and higher bulk velocities, respectively. All 8 panels in these two figures follow this format.
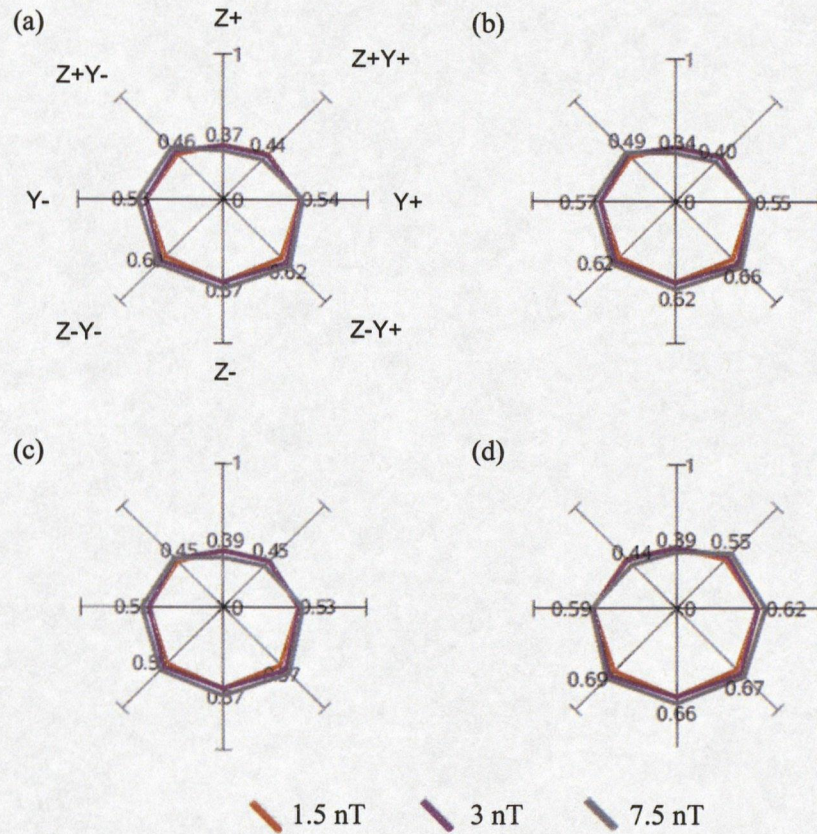
Figure 3.9. Escape Fractions sorted by IMF directions and magnitudes in the lower bulk velocity case for (a) T = 0.1eV , Dst = 0nT ; (b) T = 0.1eV , Dst= –50nT ; (c) T = 0.1eV , Dst = –90nT and (d) T = 0.2eV , Dst = 0nT.

The escape fractions are significantly lower for the lower velocity case. The higher temperature case of 0.2 eV (Figures 3.9(d) and 3.10(d)) appears to produce larger escape fractions on average, and this effect is more prominent for the lower bulk velocity. In all 8 panels in both figures, f is consistently lower for northward IMF. The effects of the dawn/dusk component of the IMF appear to be insignificant. The differences in f for B_Y positive versus B_Y negative are within 5% in all cases.
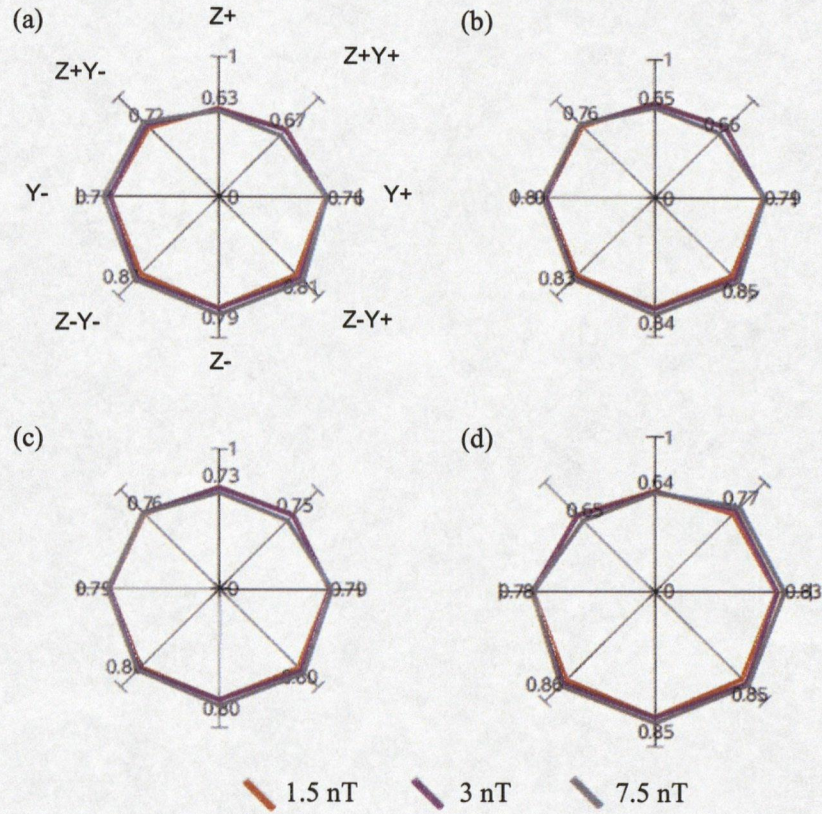
Figure 3.10. Same as Figure 3.9 but for the higher bulk velocity case.

As noted in Chapter 2, Section 2.4.1, the occurrence statistics for IMF display a fairly uniform distribution in (B_Y, B_Z). Based on this, we average f over the 8 IMF orientations. Figure 3.11 displays the escape fractions for the temperature of 0.1 eV for for both bulk velocities, sorted by Dst and IMF strength. The trapped portion for each of the cases is $n_{GT} + n_{DS}$ (gravitationally trapped and dayside particles). If the total number of particles traced is n_{total}, then the helium escape fraction is

$$(3.1) \quad f = 1 - \frac{n_{GT} + n_{DS}}{n_{total}}$$

The standard deviations on n_{GT} and n_{DS} are $\sqrt{n_{GT}}$ and $\sqrt{n_{DS}}$, respectively. Therefore, the error on f is

$$(3.2) \quad \Delta f = \frac{\Delta n_{GT} + \Delta n_{DS}}{n_{total}} = \frac{\sqrt{n_{GT}} + \sqrt{n_{DS}}}{n_{total}}$$

The error bars in Figure 3.11 were derived using this relation.
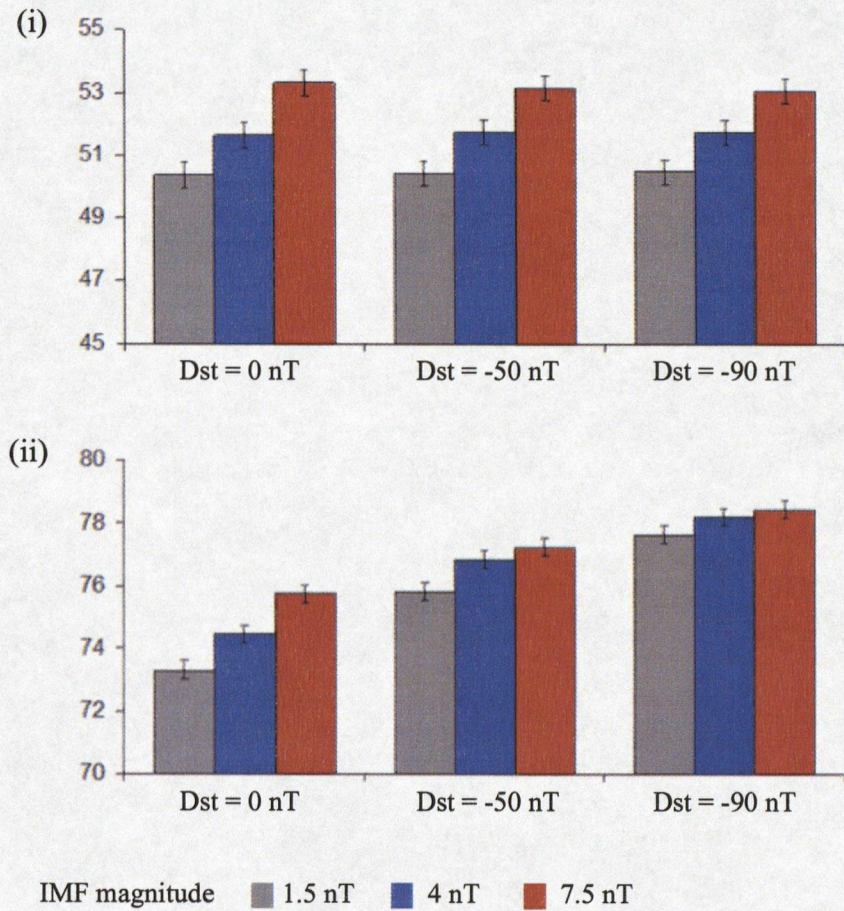
Figure 3.11. Escape fractions as a function of IMF strength and Dst at temperature 0.1eV for the (i) lower and (ii) higher bulk velocities after averaging over the 8 IMF orientations.

For the lower bulk velocity case (Figure 3.11(i)), while Dst has a negligible effect on the escape fraction, there is a positive correlation between the IMF strength and ion escape. The escape fraction for the temperature of 0.1 eV, $f_{0.1eV,L} \sim 50$ to 54% (the subscript 'L' here denotes the lower bulk velocity). For the higher bulk velocity case (Figure 3.11(ii)), the escape fraction appears to correlate with both magnetic storm activity and IMF strength, and 73% < $f_{0.1eV,H}$ < 79% (the subscript 'H' denotes the higher bulk velocity). We weight the escape fractions by the occurrence of the three levels of magnetic storm activity, which was presented in Chapter 2, Figure 2.3(b). Since the quiet time (Dst = 0 nT) fractions are weighted more strongly, the range of the weighted average for $f_{0.1eV,H}$ lies very close to the quiet time range (a difference of <1%) with $f_{0.1eV,H} \sim 73$ to 76%.

For the temperature of 0.2 eV, averaging f over all the IMF orientations,

$f_{0.2eV,L} \cong 54 - 58\%$ and $f_{0.2eV,H} \cong 75 - 78\%$. Combining the ranges of escape for both bulk velocities, our final escape fractions are

(3.3a) $f_{0.1eV} \cong 50 - 76\%$

(3.3b) $f_{0.2eV} \cong 54 - 78\%$

3.6 Escape Flux

As discussed in Chapter 1, Section 1.2, the He$^+$ flux at 1400km from Figure 1.4 [*Hoffman et al.* 1980] is $\sim 10^7$ cm^{-2}s^{-1} in the winter and $\sim 10^6$ cm^{-2}s^{-1} in the summer. Our calculation does not include the equinox flux that is bracketed by the summer and winter fluxes.

(3.2a) $F_{1400km, Winter} = 10^7 \, cm^{-2}s^{-1}$

(3.2b) $F_{1400km, Summer} = 10^6 \, cm^{-2}s^{-1}$

Our simulations are performed for particles starting at altitude 7,000 km, and we are concerned with outflow over the area above magnetic latitude 60° at that altitude, i.e. approximately ILAT 70°. The conservation of magnetic flux implies that $BA = constant$ or $B \propto A^{-1}$, where A is the area over which magnetic flux is conserved and B is the magnetic field. In the dipole approximation for the Earth's magnetic field, $B \propto R^{-3}$ where R is geocentric distance. Therefore, $A \propto R^3$. In combination with the assumption that $FA=constant$, this gives $F \propto R^{-3}$ and thus

(3.3) $F_{7000km} = \left(\dfrac{R_{1400km}}{R_{7000km}} \right)^3 \times F_{1400km}$

Equation (3.3) gives the flux at 7,000 km of $0.2 \times 10^7 \, cm^{-2}s^{-1}$ and $0.2 \times 10^6 \, cm^{-2}s^{-1}$ in the winter and the summer, respectively.

(3.4a) $F_{7000km, Winter} = 0.2 \times 10^7 \, cm^{-2}s^{-1}$

(3.4b) $F_{7000km, Summer} = 0.2 \times 10^6 \, cm^{-2}s^{-1}$

The total flux C at 7,000 km through the outflow area under consideration A_{7000km} is

(3.5a) $C = [F_{7000km, Winter} + F_{7000km, Summer}] \times A_{7000km}$

$= [F_{7000km, Winter} + F_{7000km, Summer}] \times \left(\dfrac{R_E + 7000}{R_E} \right)^3 \times A_{0km}$

Here A_{0km} is the area above ILAT 70° at the surface of the Earth, which is scaled according to $A \propto R^3$ to obtain the outflow area at 7,000 km. Multiplying this outflow flux C by our computed escape fraction f, we obtain the escape flux $C_f = f \times C$ to be

$$(3.6) \quad C_f = fC \approx (3-5) \times 10^{24} \, \text{s}^{-1}$$

In summary, our computed escape flux is $(3-5) \times 10^{24} \, \text{s}^{-1}$. This amount is in the same range as the terrestrial helium production rate of $(4.5-9.5) \times 10^{24} \, \text{s}^{-1}$ from Chapter 1, equation 1(a), and suggests that the He^+ polar wind is a dominant mechanism for terrestrial helium loss. In Chapter 4 we review the results of our study in the context of other work present in the literature, including a discussion of the validity of the methods we have used, and an assessment of the accuracy of our results.

Chapter Four: Discussion

4.1 Validity of Methods

At the beginning of our study, we surveyed the Akebono SMS data set to determine whether we could use in-situ measurement data of specific epochs and IMF conditions in our work. We identified approximately 200 orbit passes in which the observed He^+ ion count was sufficiently high and free from contamination by the other major ion species to permit analysis. However, the cases where the IMF changed significantly during an orbit pass had to be discarded since the simulation model assumes the IMF and corresponding convection electric fields to be non-varying throughout the duration of a particle trace. The simulations of both *Howarth and Yau* [2008] and *Cully et al.* [2003b] were performed for time-stationary fields rather than dynamic conditions. By this criterion, discarding the unsuitable passes for our study left less than 10 cases, which was too small to constitute a reliable data set. Therefore, we modeled the initial conditions for the ions using the Monte Carlo method and observational averages.

4.1.1 Trajectory Code

The magnetic field we use is a statistically averaged quantity. Although the IGRF and T96 models do not represent the exact field in space at any specific time, they are parameterized by observational data, and are considered accurate models for the Earth's internal and external field, respectively, and widely accepted as the best models available

for modeling studies. One of the major strengths of the *Howarth and Yau* [2008] work was the use of data-based inputs. It implemented realistic representations for the instantaneous configurations of electric field by using SuperDARN data and only selecting passes where real time data was available. Our work uses purely modeled statistical patterns which cannot account for the full range of possible convection configurations. The statistical model establishes a zero-order solution for the global convection. The maps we use are parameterized solely by IMF. In addition to IMF effects, *Ruohoniemi and Greenwald* [2005] studied seasonal effects on the convection patterns and found them to reinforce the effects of the sign of B_Y. They also studied the effect of which radar in the SuperDARN network the data was taken from. Their speculation was that the dependence on radar arose from the level of ionospheric conductivity which in turn depends on the amount of solar illumination in the radar's vicinity. Although these factors do play a role in influencing the convection patterns, they were determined to be secondary to the role of the IMF. Therefore for the purpose of this study, we have ignored effects other than those of IMF.

As discussed by *Howarth* [2006], an important drawback of the tracing model is that it does not account for a number of ion acceleration mechanisms including photoelectron effects, wave-particle interactions and collective effects of pressure gradients, thereby underestimating the net energy gain of the particles as they move along their trajectories. An additional contribution to the underestimation of the net acceleration could arise from the fact that the ambipolar parallel electric field has not been incorporated into the field model. In the altitude region where the tracing is performed, the parallel electric fields are

negligibly small compared to the perpendicular electric fields [*Howarth and Yau* 2008] and have been assumed to be zero. Another limitation to our study is the unrealistic time-independence of the fields, a consequence of modeling the IMF conditions. The code calculates the electric and magnetic fields over the spatial grid before the tracing is performed and then assumes the fields to be fixed in time. A case-by-case study including variable IMF and a reevaluation of the fields at intermediate time intervals throughout the tracing would be more precise, although it would be prohibitively time consuming.

Our tests of the trajectory code for He^+ ions were selective rather than comprehensive, limited to performing some basic tests to ensure that the model worked as expected. We rely on the tests that *Howarth* [2006] performed while developing the code. Both the field models and the integration routine were tested. The modeled magnetic field compared well to the values of the National Space Science Data Center's (NSSDC) online resource. The electric field model was tested by confirming that the magnetic field lines were correctly traced and that the calculations over the magnetospheric grid had been performed correctly. The integration method was tested by tracing particles in simple uniform field configurations and comparing the two trajectories traced by solving both the guiding center and full equations of motion. The traces for both methods overlap very closely.

4.1.2 Input to the Model

As explained in Chapter 2, Section 2.4.2, the initial conditions of the particles were set using a simplified model, distributing the initial positions uniformly in space above ILAT 70° at altitude 7,000 km and using a drifting Maxwellian distribution to select the initial velocities. In reality, the actual ion distributions are non-Maxwellian, with a higher velocity tail component in some cases [*Drakou et al.* 1997]. A Maxwellian distribution is a zero-order approximation. The *Drakou et al.* [1997] temperature study indicated that the ion temperatures lie between 0.05 to 0.35 eV, of which we performed our analysis at 0.1 and 0.2 eV. While the difference in the escape fractions calculated at the two selected temperatures was not significant, analysis for the entire range of temperatures would have to be performed in order to draw definite conclusions about the effect of temperature on the range of escape.

Typical polar wind ion outflow exists predominantly poleward of the auroral oval. The boundary of the oval is magnetic-activity dependent and lies at higher invariant latitudes on the dayside, a factor that our model does not take into account. The uniform distribution of ions above ILAT 70° is therefore an approximate characterization. The input parallel bulk velocity map we use was shown in Chapter 2, Figure 2.4. This map is a simplified adaptation of the *Abe et al.* [1993] map, shown in Chapter 1, Figure 1.6. The observed distribution exhibited a day to night asymmetry with higher velocities on the day side. The velocities peaked at auroral latitudes at all magnetic local times, i.e. at ~ 75° ILAT on the dayside and ~ 70° ILAT on the nightside.

Transport in the auroral oval has been shown to be dominated by processes other than the polar wind, which include transverse ion energization [*Whalen et al.* 1991], thermal ion upwellings [*Tsunoda et al.* 1989] and the cleft ion fountain [*Lockwood et* al. 1985]. A number of authors have studied the upflowing particle populations associated with these mechanisms. The ions have markedly different characteristics from thermal polar wind ions as a consequence of the intense energization processes they undergo, reaching energies up to a few tens of eV at altitudes a few R_E from the Earth. Our model assumes initial ion energies of a few eV or less, and while it does take into account the effects of centrifugal acceleration, it excludes energetic outflow that is produced as a consequence of the aforementioned auroral acceleration processes. The resulting error in our calculated amount of helium escape needs to be considered.

In order to calculate the error due to the exclusion of energetic outflow, we refer to the results in the work of *Collin et al.* [1988]. We introduced their work in Chapter 1, Section 1.2. Figure 1.5(a) showed the invariant latitude distribution of the occurrence frequency of energetic outflow (upflowing energetic ions, or UFI). The frequency is ~ 16 to 25% between ILAT 70° to 80°. To effectively assess the implication of neglecting energetic outflow in our analysis, we also need to consider the associated fluxes. Figure 1.5(b) showed the occurrence frequency distribution of the He^+ UFI (with H^+ and O^+ for comparison) as a function of the upward integrated flux normalized to 1,000 km altitude. The He^+ flux mostly lies below 3×10^7 $cm^{-2}s^{-1}$, though it does at times exceed 10^8 $cm^{-2}s^{-1}$. It falls off at ~ 2×10^7 $cm^{-2}s^{-1}$, and we use this amount in our calculation of the energetic

helium ion density. The energy range lies between ~ 0.01 to 1 keV , i.e. the average ion

energy and velocity are ~ 0.1 keV and ~ 70 km/s, respectively. The density is therefore

$n_{Energetic} \cong 3 \, cm^{-3}$. As shown in Figures 1.4(a) and 1.4(b) in Chapter 1, the thermal helium

ion density at 1400 km between ILAT 70° to 80° [*Hoffman and Dodson* 1980] lies

between $10^1 \, cm^{-3}$ in summer and $10^2 \, cm^{-3}$ in winter. Comparing the energetic and thermal

ion densities, $n_{Energetic} / n_{Thermal}$ lies between 3 and 30%. The escape fraction calculated at

temperature 0.1eV is $f_{0.1eV} \cong (50-76)\%$ (Chapter 3, Section 3.5). The fraction of

particles that do not escape is therefore $f'_{0.1eV} = (50-24)\%$. A higher limit estimate of

the effect of neglecting energetic outflow on our result would assume $f'_{0.1eV}$ to be subject

to the error discussed above, with a component that is in fact energetic and able to escape.

However, considering the occurrence frequency (16 to 25%) in combination with the

density ratio (3 to 30%) gives the error to be limited to less than 4% (where the auroral-

oval-to-polar-cap surface area ratio has also been taken into account). This error is not

significant.

4.2 Previous work

In Chapter 1, Section 1.2, we cited the work of *Lie-Svendsen and Rees* [1996] that also

addressed the question of the imbalance in the terrestrial helium budget and its

relationship to helium outflow through the polar wind. However, their method for

quantifying the helium escape was based on a number of theoretical assumptions about

polar wind outflow that are inconsistent with results from other studies in the literature,

as discussed below. In comparison, in this study, our method of analysis is based on simulated He$^+$ trajectories and destination distributions using observational data derived from SuperDARN and satellite measurements.

Lie-Svendsen and Rees [1996] modeled the production of He$^+$ from the photoionization of neutral helium, assuming the initial ion velocities to be purely thermal and represented by a Maxwellian distribution at the neutral helium temperature, and ignoring convection electric fields. Their justification for excluding horizontal transport was that since the diurnal variation of the electric field is partially a function of universal time (UT), by averaging their final results over UT they diminish the effect of convection. In their first paper, they used a combination of kinetic theory and standard moment equations based on the above assumptions. They concluded that the primary factor influencing the helium outflow flux was the transition altitude between the region of chemical equilibrium (below) and where loss due to charge exchange reactions became insignificant (above). In their second paper, they developed a computationally efficient 'shortcut' method to compute global He$^+$ escape fluxes based on this conclusion from their previous work.

For a range of diurnal, seasonal, universal time and solar activity geophysical conditions, they identified the altitude at which the transport dominated region began, i.e. where local loss ceased to be important compared to the production due to photoionization. They defined this altitude to be the height above which the integrated column production rate is equal to the escape flux at the top, assuming the production rate above the transition altitude would be balanced by the polar wind outflow. For an estimate of global helium

escape flux, they averaged over the conditions listed above and calculated the global distribution of the column production rate above the transition altitude. They divided the surface of the Earth into 50×50 grid points spaced equally in latitude and longitude. Since loss due to the polar wind only occurs in high latitude regions, they considered a range of cut-off latitudes between 50° to 70° and in each case they calculated the corresponding column production rate over the grid points enclosed in the selected surface area. They divided the resultant amount by the entire surface area of the Earth to obtain the mean production rate. This was compared to the outgassing rate of helium from the Earth's crust. By their calculations, a latitude cut-off of 60° or lower is sufficient to balance the terrestrial production rate of helium.

The principal drawback to the analysis of *Lie-Svendsen and Rees* [1996] is that the underlying assumptions in their analysis do not support their supposition that outflow through the polar wind would balance the column production rate. First, their assumption of a (non-drifting) Maxwellian distribution resulted in an underestimation of the ion energies, since in general helium ions in the polar wind have non-zero drift velocities in the field-aligned direction in addition to their thermal velocities. A more accurate representation of the initial helium ion velocities is provided by a drifting Maxwellian distribution. Second, the assumption of no horizontal transport neglects the significant effect of centrifugal acceleration that occurs as a consequence of the perpendicular electric fields present in altitude regions of large magnetic field curvature (i.e. at high altitudes) in the high latitude ionosphere. The process of centrifugal acceleration is one of the most important processes responsible for the transport of ionospheric plasma to the

magnetosphere [*Cladis* 1986; *Cladis et al.* 2000], and neglecting it would result in significant underestimation of outflow flux. *Lie-Svendsen and Rees* [1996] assumed that the height-integrated helium ion production rate over the polar cap equates to the escape flux, which appears inconsistent with the assumptions of no horizontal and (bulk) vertical transport and the resulting reduction in escape flux. They found that in their case of no horizontal and vertical transport a cut-off (geographic) latitude of 60° is required for the integrated escape flux (above the cut-off latitude) to balance the ion production rate. However, it is clear from observations (see for example Figures 1.4 and 1.6) that a cut-off of 60° represents a significant overestimation of the area covered by the polar wind.

Our work constitutes the first semi-empirical approach to study He^+ outflow in order to explain the terrestrial helium budget. As first discussed in Section 2.1.2 and subsequently throughout this thesis, our study follows the studies of *Howarth and Yau* [2008] and *Cully et al.* [2003b], solving the same set of guiding center equations (for He^+ rather than H^+ and O^+ ions) and tracing single particle trajectories in space to study ion outflow through the polar ionosphere. Since polar wind ions characteristically have velocities which vary inversely with their mass, any He^+ results are in general expected to be bracketed by those for H^+ and O^+. However, differences in the objectives and input in the two previous studies make a quantitative comparison of this nature difficult. Rather than obtaining a statistically averaged rate of outflow, they studied the dynamics of outflowing ions under specific geophysical conditions. *Cully et al.* [2003b] investigated the supply of ionospheric ions to the central plasma sheet, taking into account ions that have already escaped the Earth's gravitational field. We have been able to compare our results to those

obtained by *Howarth and Yau* [2008] more easily. They investigated the effect that IMF and convection electric field have on outflowing ions, including gravitationally trapped ions in their output distributions. The average fraction of gravitationally trapped ions we obtained at temperature of 0.1 eV for He^+ clearly lies between their fractions for H^+ and O^+ at the same temperature. We have defined our fraction of trapped particles to be those that are gravitationally trapped or transported to the dayside. The latter fraction is significantly lower than the former, and our comparison of the trapped fractions between the two studies is sufficient to conclude that the He^+ escape is bracketed by the H^+ and O^+ escape.

Conclusion

The goal of our work was to determine whether the helium escape associated with helium

ions in the polar wind could explain the problem of the terrestrial helium budget. To do

so, it is sufficient to bracket the range of escape over a variety of geophysical conditions.

By simulating the trajectories and destinations of particles using a single-particle tracing

model and analyzing the source and destination distributions of the simulated trajectories,

we identified a number of characteristics of the helium polar wind. We found that the

average distribution of ions to different regions in the magnetosphere was qualitatively

very similar for different IMF strengths and Dst conditions. The number of

gravitationally trapped ions was significantly higher for a lower bulk velocity. In

agreement with results obtained by *Howarth and Yau* [2008], the fraction of trapped ions

was also higher for northward (orientations $+Z$, $+Z+Y$ and $+Z-Y$) versus southward

(orientations $-Z$, $-Z+Y$ and $-Z-Y$) IMF. The outflow area we considered was poleward of

ILAT 70°. Averaged over IMF magnitude and direction, and weighted by the occurrence

distribution of Dst, the global escape fraction through this area for the ion temperature of

0.1 eV was found to be $f_{0.1eV} \cong 50-76\%$. For the temperature of 0.2 eV,

$f_{0.2eV} \cong 54-78\%$ at magnetically quiet times. We calculated the outflow flux through

the given area based on the observation results of *Hoffman and Dodson* [1980].

Combining the escape fraction with the outflow flux, our estimate for the escape flux is

$\sim (3-5) \times 10^{24} \, \text{s}^{-1}$. Comparing our estimated rate of escape to the atmospheric helium

production rate of $\sim (4.5-9.5) \times 10^{24} \, \text{s}^{-1}$, we conclude that the polar wind is indeed a very

likely mechanism to account for the balance between the sources and sinks of terrestrial helium.

A number of improvements can be made to our study for a more precise calculation of the helium escape. A more accurate adaptation of the *Abe et al.* [1993] velocity map could be used as input to the model. A larger set of temperature-Dst cases could be considered, including the full range of thermal ion temperatures reported by *Drakou et al.* [1997]. Some case studies based on in-situ measurement data could be performed for a comparison to our statistically averaged results. Seasonal effects and the effect that the dipole tilt has on the escape could be taken into account. Some of the acceleration mechanisms that we have neglected could be explored, to determine whether they could be incorporated into the tracing model. These include wave-particle interactions, photoelectron effects, parallel electric fields and other auroral energization processes. Finally, although He^3 is mostly of extra-terrestrial origin and its production rate is balanced by thermal Jeans escape, it might be interesting (though extremely challenging because of the small isotope ratio) to investigate the significance of its outflow through the polar wind.

Bibliography

Abe, T., B. A. Whalen, A. W. Yau, R. E. Horita, S. Watanabe, and E. Sagawa, EXOS-D (Akebono) Suprathermal Mass Spectrometer observations of the polar wind, *J. Geophys. Res.*, *98*, 11,191, 1993.

Andersson, L., W.K. Peterson, and K.M. McBryde, Dynamic coordinates for auroral ion outflow, *J. Geophys. Res.*, *109 (A08201)*, doi:10.1029/2004JA010424, 2004.

Axford, W. I., The polar wind and the terrestrial helium budget. *J. geophys. Res.*, *73*, 6855, 1968.

Banks, P. M., and T. E. Holzer, High-Latitude Plasma Transport: The Polar Wind, *J. Geophys. Res.*, *74*, 6317, 1968.

Bates, D. R., and M.R.C. McDowell, Atmospheric helium, *J. Atmos. Terr. Phys.*, *11*, 200, 1957.

Baumjohann, W., and R. A. Treumann, *Basic Space Plasma Physics*, Imperial College Press, London, England, 1997.

Brankin, R. W., and I. Gladwell, RKSUITE 90.doc, *Tech. rep.*, Numerical Algorithms Group Ltd., Wilkinson House, Jordan Hill Road, Oxford, U.K., 1995.

Cladis, J. B., Parallel acceleration and transport of ions from polar ionosphere to plasma

sheet, *Geophys. Res. Lett., 13* , 893, 1986.

Cladis, J. B., H. L. Colin, O. W. Lennartsson, T. E. Moore, W. K. Peterson, and C. T.

Russell, Observations of centrifugal acceleration during compression of the

magnetosphere, *Geophys. Res. Lett., 27* , 915, 2000.

Collin, H.L., W.K. Peterson, J.F. Drake, and A.W. Yau, The Helium Components of

Energetic Terrestrial Ion Upflows: Their Occurrence, Morphology, and Intensity, *J.

Geophys. Res., 93*, 7558, 1988.

Cully, C. M., Observations and trajectory simulations of terrestrial ion outflow, *Master's

thesis*, University of Calgary, Calgary, AB, 2001.

Cully, C. M., E. F. Donovan, A. W. Yau, and G. G. Arkos, Akebono/Suprathermal

Mass Spectrometer observations of low-energy ion outflow: Dependence on magnetic

activity and solar wind conditions, *J. Geophys. Res., 108*, 1093, 2003a.

Cully, C. M., E. F. Donovan, A. W. Yau, and H. J. Opgenoorth, Supply of thermal

ionospheric ions to the central plasma sheet, *J. Geophys. Res., 108*, 1092, 2003b.

Delcourt, D. C., C. R. Chappell, T. E. Moore, and J. H. Waite Jr., A three-dimensional

numerical model of ionospheric plasma in the magnetosphere, *J. Geophys. Res., 94*, 11,893, 1989.

Delcourt, D. C., J. A. Sauvaud, and T. E. Moore, Polar wind ion dynamics in the magnetotail, *J. Geophys. Res., 98*, 9155, 1993.

Delcourt, D. C., T. E. Moore, and C. R. Chappell, Contribution of low-energy ionospheric protons to the plasma sheet, *J. Geophys. Res., 99*, 5681, 1994.

Delcourt, D. C., and G. Belmont, Particle dynamics in the near-earth magnetotail and macroscopic consequences, in *New Perspectives on the Earth's Magnetotail, Geophys. Monogr. Ser.*, vol. 105, edited by A. Nishida et al., pp. 193, AGU, Washington, D. C., 1998.

Drakou, E., A. W. Yau, and T. Abe, Ion temperature measurements from the Akebono Suprathermal Mass Spectrometer: Application to the polar wind, *J. Geophys. Res., 102*, 17,523, 1997.

Greenwald, R. A., K.B. Baker, J.R. Dudeney, M. Pinnock, T.B. Jones, E.C. Thomas, J.-P. Villain, J.-C. Cerisier, C. Senior, C. Hanuise, R.D. Hunsucker, G.Sofko, J. Koehler, E. Nielson, R. Pellinen, A.D.M Walker, N. Sato, and H. Yamagishi, DARN/SUPERDARN: A global view of the dynamics of high-latitude convection, *Space Sci. Rev., 71*, 761, 1995.

Hedin, A.E., MSIS-86 thermospheric model, *J. Geophys. Res.*, *92*, 4649, 1987.

Hedin, A.E., J.E. Salah, J.V. Evans, C.A. Reber, G.P. Newton, N.W. Spencer, D.C. Kayser, D. Alcayde, P. Bauer, L. Cogger, and J.P. McClure, A Global Thermospheric Model Based on Mass Spectrometer and Incoherent Scatter Data, MSIS 1. N_2 Density and Temperature, *J. Geophys. Res.*, *82*, 2139, 1977.

Hedin, A.E., C.A. Reber, G.P. Newton, N.W. Spencer, H.C. Brinton, H.G. Mayr, and W.E. Potter, A Global Thermospheric Model Based on Mass Spectrometer and Incoherent Scatter Data, MSIS 2. Composition, *J. Geophys. Res.*, *82*, 2148, 1977.

Hoffman, J. H., Studies of the composition of the ionosphere with a magnetic deflection mass spectrometer, *Int. J. Mass Spectrom., Ion Phys.*, *4*, 315, 1970.

Hoffman, J. H., and W. H. Dodson, Light ion concentrations and fluxes in the polar regions during magnetically quiet times, *J. Geophys. Res.*, *85*, 626, 1980.

Hoffman, J. H., W. H. Dodson, C. R. Lippincott, and H. D. Hammack, Initial ion composition results from the ISIS 2 satellite, *J. Geophys. Res.*, *79*, 4246, 1974.

Horwitz, J.L., and M. Lockwood, The cleft ion fountain: a two-dimensional kinetic model, *J. Geophys. Res.*, *90*, 9749, 1985.

Howarth, A., Polar Wind Transport Under Various Interplanetary Magnetic Field Conditions, *Master's thesis*, University of Calgary, Calgary, AB, 2006.

Howarth, A., and A.W. Yau, The effects of IMF and convection on thermal ion outflow in magnetosphere - ionosphere coupling, *J. Atmos. Sol. Terr. Phys.*, doi:10.1016/j.jastp.2008.08.008, 2008.

Huddleston, M.M., C.R. Chappell, D.C. Delcourt, T.E. Moore, B.L. Giles, and M.O. Chandler, An examination of the process and magnitude of ionospheric plasma supply to the magnetosphere, *J. Geophys. Res.*, *110*, A12202, doi:10.1029/2004JA90401, 2005.

Keating, G.M., and E.J. Prior, The winter helium bulge, *Space Res. VIII*, 982, 1970.

Kockarts, G., Helium in the terrestrial atmosphere, *Space Sci. Rev.*, *14*, 723, 1973.

Leer, E., O. Lie-Svendsen, E.L. Olsen, and V.H. Hansteen, Outflow of He^+ from the polar ionosphere: Comparison of hydrodynamic and kinetic descriptions, *J. Geophys. Res.*, *101*, 17207, 1996.

Lemaire, J., O^+, H^+ and He^+ ion distributions in a new polar wind model, *J. Atm. Terr. Phys.*, *34*, 1647, 1972.

Lie-Svendsen, O., M. H. Rees, and K. Stamnes, Helium escape from the Earth's atmosphere: The charge exchange mechanism revisited, *Planet. Space Sci., 40*, 1639, 1992.

Lie-Svendsen, O., and M. H. Rees, An improved kinetic model for the polar outflow of a minor ion, *J. Geophys. Res., 101*, 2415, 1996.

Lie-Svendsen, O., and M. H. Rees, Helium escape from the terrestrial atmosphere: The ion outflow mechanism, *J. Geophys. Res., 101*, 2435, 1996.

Lockwood, M., M. Chandler, J. Horwitz, J. Waite Jr., T. Moore, and C. Chappell, The Cleft Ion Fountain, *J. Geophys. Res., 90(A10)*, 9736, 1985.

MacDonald, G. J. F., The escape of helium from the Earth's atmosphere, *Rev. Geophys., 1*, 305, 1963.

Maier, W.B., II, Reactions of He+ with N2 and O2 in the upper atmosphere, *Planet. Space Sci., 16*, 477, 1968.

Mayr, H.G., E.G. Fontheim, L.H. Brace, H.C. Brinton, and H.A. Taylor, A theoretical model of the ionosphere dynamics with interhemispheric coupling, *J. Atmos. Terr. Phys., 34*, 1659, 1972.

Nicolet, M., The aeronomic problem of helium, *Ann. Geophys.*, *13*, 1, 1957.

Nicolet, M., Helium, an important constituent in the lower exosphere, *J. Geophys. Res.*, *66*, 2263, 1961.

Northrop, T. G., *The Adiabatic Motion of Charged Particles*, Wiley-Interscience, New York, 1963.

Patterson, T.N.L., Escape of atmospheric helium by nonthermal processes, *Rev. Geophys.*, *6*, 553, 1968.

Press, W. H., S. A. Teukolsky, W. T. Vetterling, and B. P. Flannery, eds., *Numerical Recipes in Fortran, The Art of Scientific Computing*, pp. 650, 2nd ed., Cambridge Univ. Press, New York, 1992.

Raitt, W.J., and R.W. Schunk, Composition and characteristics of the polar wind, In: Johnson, R.G. (Ed.), *Energetic Ion Composition in the Earth's Magnetosphere*, Terra Scientific Publishing, Tokyo, 99, 1983.

Raitt, W.J., R.W. Schunk, and P.M. Banks, Helium ion outflow from the terrestrial ionosphere, *Planet. Space Sci.*, *26*, 255, 1978a.

Raitt, W.J., R.W. Schunk, and P.M. Banks, Qualitative calculations of helium ion escape fluxes from the polar ionospheres, *J.Geophys. Res.*, *83*, 5617, 1978b.

Reiff, P.H., The Sun-Earth Connection, http://space.rice.edu/IMAGE/livefrom/sunearth.html, 1999.

Ruohoniemi, J. M., and K. B. Baker, Large-scale imaging of high-latitude convection with Super Dual Auroral Radar Network HF radar observations, *J. Geophys. Res.*, *103*, 20,797, 1998.

Ruohoniemi, J. M., and R. A. Greenwald, Statistical patterns of high-latitude convection obtained from Goose Bay HF radar observations, *J. Geophys. Res.*, *101*, 21,743, 1996.

Ruohoniemi, J. M., and R. A. Greenwald, Dependencies of high-latitude plasma convection: Consideration of interplanetary magnetic field, seasonal, and universal time factors in statistical patterns, *J. Geophys. Res.*, *110*, A09204, doi: 10.1029/2004JA010815, 2005.

Ruohoniemi, J. M., R. A. Greenwald, K. B. Baker, J.-P. Villain, and M. A. McCready, Drift motions of small-scale irregularities in the high-latitude *F* region: An experimental comparison with plasma drift motions, *J. Geophys. Res.*, *92*, 4553, 1987.

Shepherd, S. G., and J. M. Ruohoniemi, Electrostatic potential patterns in the high latitude ionosphere constrained by SuperDARN measurements, *J. Geophys. Res.*, *105*, 23,005, 2000.

Torgersen, T., Terrestrial helium degassing fluxes and the atmospheric helium budget: implications with respect to the degassing processes of continental crust, *Chem. Geol. (Isot. Geosci. Sect.)*, *79*, 1, 1989

Tsunoda, R.T., R.C. Livingston, J.F. Vickrey, R.A. Heelis, W.B. Hanson, F.J. Rich, and P.F. Bythrow, Dayside observations of thermal-ion upwellings at 800-km altitude: An ionospheric signature of the Cleft Ion Fountain, *J. Geophys. Res.*, *94*, 15277, 1989.

Tsyganenko, N. A., A magnetospheric magnetic field model with a warped tail current sheet, *Planet. Space Sci.*, *37*, 5, 1989.

Tsyganenko, N. A., Modeling the Earth's magnetospheric magnetic field confined within a realistic magnetopause, *J. Geophys. Res.*, *100*, 5599, 1995.

Tsyganenko, N. A., and D. P. Stern, A new-generation global magnetosphere field model, based on spacecraft magnetometer data, *ISTP Newsletter*, *6*, 21, 1996.

Weimer, D. R., Models of high latitude electric potentials derived with a least error fit of spherical harmonic coefficients, *J. Geophys. Res.*, *100*, 19,595, 1995.

Whalen, B., S. Watanabe, and A. Yau, Observations in the transverse ion energization region, *Geophys. Res. Lett.*, *18(4)*, 725, 1991.

Winglee, R. M., Mapping of ionospheric outflows into the magnetosphere for varying IMF conditions, *J. Atmos. Terr. Phys.*, *62*, 527, 2000.

Yau, A.W., and M. Andre, Sources of ion outflow in the high latitude ionosphere, *Space Science Review*, *80(1–2)*, 1, 1997.

Yau, A. W., B. A. Walen, W. K. Peterson, and E.G. Shelley, Distribution of upflowing ionospheric ions in the high-altitude polar cap and auroral ionosphere, *J. Geophys. Res.*, *89*, 5507, 1984.

Yau, A. W., P. H. Beckwith, W. K. Peterson, and E.G. Shelley, Long-term (solar-cycle) and seasonal variations of up(lowing ionospheric ion events at DE-1 altitudes, *J. Geophys. Res.*, *90*, 6395, 1985a.

Young, D. T., H. Balsiger, and J. Geiss, Correlations of magnetospheric ion composition with geomagnetic and solar activity, *J. Geophys. Res.*, *87*, 9077, 1982.